Attachment of CeO_2 and SiO_2 for Chemical Mechanical Polishing: Theory and Experiments

by

Elham Rafie Borujeny

A thesis submitted in partial fulfillment of the requirements for the degree of

Master of Science

in

Chemical Engineering

Department of Chemical and Materials Engineering
University of Alberta

Abstract

Interactions of finely dispersed abrasive particles in chemical mechanical planarization (CMP) slurries play a vital role in determining the polishing performance. In this study, coupled influence of hydrodynamic and colloidal interactions on the attachment of nanosized ceria (CeO_2) particles to a silica (SiO_2) surface is investigated. Deposition rates of ceria nanoparticles on silica sensor are determined using quartz crystal microbalance with dissipation monitoring (QCM-D) as a model system and compared with theoretical transport models under the influence of colloidal interactions. It is found that the deposition of ceria nanoparticles on silica is highly dependent on the solution pH, fluid velocity, and concentration of ceria particles in the solution. The system is shown to exhibit considerably different behaviors at acidic and basic pH conditions. More specifically, stronger attachment occurs at neutral pH conditions than at acidic or basic conditions. The concentration of particles is also shown to affect the interaction of ceria with silica in a complex way which is not necessarily predictable by the simplified theories of colloidal interactions. More specifically, increasing ceria bulk concentration within some ranges results in decreasing the initial deposition rate.

To my parents,

And my brothers, Arash and Reza.

Acknowledgements

Doing a research work begins with a great deal of individual excitement but it will never finish without the support of many other people. This work has also benefited from contributions of many individuals.

First and foremost, I would like to express my sincere gratitude to my supervisors, Dr. Kenneth Cadien and Dr. Zhenghe Xu, for their support, patience, and encouragement. This work would not have been possible without their persistent help.

My very special thanks goes to Dr. Ali Khademhosseini at Harvard-MIT Division of Health Sciences and Technology, without his kind advice I would not have considered studying chemical engineering. I thank him for letting me know that the trick was to remain motivated and passionate.

I acknowledge my leaders and peers for sharing their ideas and expertise with me. I thank the faculty and staff of Departments of Chemical and Materials Engineering, Mechanical Engineering, and Chemistry at the University of Alberta who provided me their knowledge, technical expertise, and administrative support.

Last but not least, I gratefully thank my parents, my dearest aunt, and my brothers for listening, offering me advice, and supporting me during every single moment of my studies even when we were physically thousands of miles away. I thank my beloved brother, Reza, for contributing ideas, interpretations, offering me endless support, and taking care of everything in our lives while I was doing this work.

Contents

List of Tables

List of Figures

List of Symbols

List of commonly used symbols

A_H	Effective Hamaker Constant $[J]$
a_p	Particle Radius $[m]$
C_f	Friction Coefficient $[\frac{Ns}{m}]$
D or $\bar{\bar{D}}$	Diffusion Coefficient $[\frac{m^2}{s}]$
D_∞	Diffusion Coefficient $[\frac{m^2}{s}]$
D_p	Particle Diameter $[m]$
d	Distance of Closest Approach Between Moieties $[m]$
d_0	Cut-off Distance to Account for Born Repulsion $[m]$
$h = \frac{z}{a_p} - 1 = \frac{d}{a_p}$	Dimensionless Distance
j_D	Diffusive Flux of Particles $[\frac{mol}{m^2.s}$ or $\frac{\#}{m^2.s}]$
k_B	Boltzmann Constant $(1.381\times10^{-23}$ $[\frac{J}{K}])$
k_a	Adsorption or Attachment Rate Constant
k_d	Desorption or Release Rate Constant
n	Molar or Number Concentration of Particles $[\frac{mol}{m^3}$ or $\frac{\#}{m^3}]$
Q	Source Term in Convection-Diffusion Equation $[\frac{mol}{m^3.s}$ or $\frac{\#}{m^3.s}]$
R	QCM-D Response $(f$ or $D)$
T	Temperature $[K]$
t	Time $[s]$
γ	Surface Tension $[\frac{J}{m^2}]$
ϵ	Dielectric Permitivity $[\frac{C}{Vm}]$
ϵ_0	Dielectric Permitivity of Vacuum $(8.854\times10^{-12}$ $[\frac{C}{Vm}])$
ϵ_r	Relative Permitivity $[dimensionless]$
κ	Inverse Debye Screening Length $[m^{-1}]$

λ	Characteristic Decay Length of Acid-Base Interactions $[m]$
μ	Bulk Fluid Viscosity $[Pa.s = \frac{kg}{s.m}]$
ρ	Density $[\frac{kg}{m^3}]$
σ	Surface Charge Density $[\frac{C}{m^2}]$
ψ_c	Surface Potential of Collector/Sensor $[V]$
ψ_p	Surface Potential of Particles $[V]$

List of Abbreviations

List of commonly used abbreviations

AB	Acid-Base
CMP	Chemical Mechanical Planarization
DLS	Dynamic Light Scattering
DLVO	Derjaguin-Landau-Verwey-Overbeek
EDL	Electric Double Layer
IC	Integrated Circuit
MAS	Mixed Abrasive Slurry
MRR	Material Removal Rate
NP	Nanoparticle
PALS	Phase Analysis Light Scattering
PB	Poisson Boltzmann
PDI	Poly-Dispersity Index
PSD	Particle Size Distribution
QCM-D	Quartz Crystal Microbalance with Dissipation monitoring
STI	Shallow Trench Isolation
vdW	van der Waals
XDLVO	Extended DLVO

Chapter 1

Introduction

1.1 Background

Chemical Mechanical Planarization (CMP) is a global planarization technique which can produce extremely flat and smooth surfaces by the synergistic effect of complex chemical and mechanical processes. CMP has many applications in a wide range of areas of nanofabrication including semiconductor industry for integrated circuit (IC) manufacturing [2]. While early ICs contained only a handful of devices, today's microprocessors contain more than one billion transistors in a chip area of approximately 3 cm × 3 cm. Integration of large numbers of transistors into a small chip in close proximity requires sophisticated techniques to electrically isolate them. Shallow Trench Isolation (STI) process is a technique used for this purpose. STI is a "front end" process (i.e., happens at the transistor level) and it provides improved control over the geometry of the isolated area. Hence, it enhances the planarization dramatically and enables higher packing density of transistors in ICs. The key steps of the STI process involve depositing a silicon nitride masking layer on the silicon substrate, etching a pattern of trenches in the silicon nitride and silicon, depositing silicon dioxide (as a dielectric materials) to fill the trenches, and using CMP to remove the SiO_2 overburden, while stopping on Si_3N_4.

The outcome of the CMP process depends on the mutual interactions of several factors, including [3]:

1. Surfaces involved in the process (i.e., the surface to be polished and the polishing pad);
2. Abrasive particles in the slurry (i.e., particle type, size, morphology and concentration);
3. Chemical additives in the slurry (i.e., to adjust the slurry pH and/or to serve as oxidizer, chelating agent, etc.).

Two major types of slurries are used in STI CMP. They are slurries that use silica or ceria particles as abrasives. While ceria based slurries have the advantage of higher oxide to nitride selectivity over silica based slurries [4, 5, 6, 7, 8, 9], it has been recently shown by Lin et al. [1] that material removal rate (MRR) is dramatically increased when using mixed abrasive slurries (MAS). A number of studies have been conducted on the polishing performance of mixed abrasive slurries [1, 10, 11, 12, 13, 14, 15]. However, only a few studies have focused on CMP by mixed ceria and silica slurries and even fewer have related dispersion stability of these slurries to the electrokinetic properties of the dispersed particles. Lin et al. [1] studied the colloidal stability of ceria-silica MAS prepared by simply mixing the individual slurries and correlated the improved CMP performance using such slurries to the interactions of particles in the MAS. It was shown that these interactions are affected by the surface charge properties of the particles. Such mixed abrasive slurries exhibit different stability at pH 4 and 10 which are on the two sides of the isoelectric point of ceria particles. However, there are other factors involved that make the understanding and controlling of nanoparticle (NP) interactions more complex. Although some researchers have characterized the electrokinetic and transport properties of silica and ceria nanoparticles by traditional laboratory experiments such as settling tests, column tests, and light transmittance tests [1, 16, 17], our understanding of interactions in the mixture of these particles remains incomplete and requires more elaboration. Further elucidation of the interactions in the mixture of these particles requires comprehensive studies using different approaches and techniques which should, when combined, produce criteria for tailoring CMP slurries.

1.2 Goal of This Work

This work is a fundamental study of the interactions of ceria nanoparticles with silica using Quartz Crystal Microbalance with Dissipation monitoring (QCM-D), which allows real time monitoring of interactions taking place at surfaces. Ceria slurry from Nyacol Nanotechnologies is used to study the attachment of CeO_2 particles to SiO_2 surface as a function of time at different flow rate, pH, and NP concentration. The current study provides insight into the deposition kinetics of the aforementioned system and highlights the importance of different conditions such as pH, particle type, particle size, flow and static environment on nanoparticle interactions from both theoretical and experimental point of view. To this end, colloid deposition dynamics is investigated by conducting a series of well-controlled experiments under different flow rate, particle concentration and pH conditions. Furthermore, a mathematical transport model is developed, which accounts for both hydrodynamic and non-hydrodynamic interactions. Then, using the experimentally measured parameters of the system (such as particle charge and size), the model is numerically solved and its ability to explain the experimental data is assessed.

As part of this study, a method was developed for cleaning and preparing QCM-D sensors prior to experiments. In addition to finding optimum cleaning conditions for reusability of QCM-D sensors, interpretation of QCM-D data when studying the deposition of NPs is discussed in this thesis.

1.3 Outline of Thesis

A brief introduction to the importance of studying the attachment of ceria and silica is presented in the current chapter (Chapter 1).

Chapter 2 reviews and discusses the interaction forces acting in the system. Two different deposition scenarios are explained in in this chapter. A detailed explanation of two approaches for analyzing the interaction energies of monolayer deposition is given, and the applicability of each approach to the silica-ceria interaction is examined. In addition, governing transport equations for the deposition of ceria onto silica using a QCM-D apparatus are derived and numerically solved. Finally, a procedure for analyzing raw QCM-D data and comparing them with numerical results is presented.

Chapter 3 outlines the experimental procedures, and provides information on the instruments and software used in this work.

Chapter 4 explores the optimum experimental conditions for conducting QCM-D experiments and suggests improved cleaning protocols for the QCM-D sensors. This chapter proposes simple tips to identify possible sources of error and to improve reproducibility of QCM-D experimental results. In addition, it illustrates the experimental results and demonstrates the use of the models derived in Chapter 2 in explaining the observed behavior of the system.

Lastly, Chapter 5 concludes this work and provides suggestions for future work. Also outlined in this chapter is an extended governing transport equation which, with more elaboration, can be used to address some of the limitations of the current methods of QCM-D data analysis.

Chapter 2

Theoretical Background

In this chapter, the theoretical background for studying NPs interactions will be discussed. The discussion mainly lies within the scope of colloid and interface science. The forces which are generally involved in creating the flux of NPs in a deposition (and/or coagulation) process are discussed in Section 2.1. Theoretically, these forces can promote the formation of either a monolayer or a multilayer of colloidal particles on the surface of a collector (which can be either a planar surface or particles that are considerably larger than the suspended particles). A brief explanation on modeling each of these cases (i.e. multilayer vs monolayer deposition) is presented in Section 2.2. Section 2.3 describes, in detail, the appropriateness of the monolayer deposition model in investigating the attachment of ceria NPs to flat silica surface. It will be explained how different interaction forces are combined to form the well-known Derjaguin-Landau-Verwey-Overbeek (DLVO) theory, which is then used to analyze the colloidal interaction from a thermodynamic point of view. Extending DLVO theory, XDLVO (also known as EDLVO) theory will be discussed and its applicability to the study of the interaction of ceria and silica will be assessed. Section 2.4 is devoted to the study of the dynamics of interactions of ceria and silica. A comprehensive picture of the transport of ceria particles in the vicinity of a flat silica surface will be presented, which is then used to mathematically model the deposition phenomenon taking place in QCM-D.

2.1 Involved Forces (How is the flux of particles created?)

When a particle successfully collides with and attaches to a much larger particle or a surface (referred to as *collector*), the process is called deposition. Deposition of flowing colloidal particles onto a stationary, large collector occurs due to the combination of:

- Brownian motion
- Hydrodynamic interactions
- Gravitational forces
- van der Waals forces
- Electric double-layer (electrostatic) forces

The study of this phenomenon requires a knowledge of these forces as well as the flow field around the collector, which affects the rate of collision between the particles as well as between the particles and collector.

2.1.1 Brownian Motion

Brownian motion of colloidal particles in a suspension is created by the collective effect of thermal motion of the liquid molecules. Brownian motion should be taken into consideration when investigating deposition of sub-micron sized particles as it is known to be the primary mechanism to induce collision and subsequent attachment, or deposition, during flow past the surface of a collector. Brownian motion is closely related to and usually explained in conjunction with the diffusion coefficient (D) of the colloidal particles. Fick's first law employs the diffusion coefficient to relate diffusive flux of particles (j_D) to their concentration gradient (∇n) by stating that in the presence of a concentration gradient, the particles move from regions of high concentration to regions of low concentration by diffusion:

$$j_D = -D\nabla n \tag{2.1}$$

However, it should be noted that even in the case of the absence of a concentration gradient, Brownian motion does not cease and the particles still wander randomly in the solution. The only difference is that random motion of the particles will not cause a net directional flux as a macroscopic manifestation.

At infinite dilution and in the absence of surface charge, a constant diffusion coefficient can be assigned to a spherical particle of radius a_p suspended in a fluid of viscosity μ by Stokes-Einstein equation:

$$D = D_\infty = \frac{k_B T}{C_f} = \frac{k_B T}{6\pi\mu a_p} \tag{2.2}$$

where $C_f = 6\pi\mu a_p$ is the Stokes coefficient of friction, and D is assumed to be unaffected by the presence of the surrounding particles. C_f should be corrected to take the proximity of other objects into account. Corrections for the presence of stationary surfaces in low Reynolds number regimes are studied in literature [18, 19, 20, 21, 22] and will be discussed in more detail in Section 2.4.1. Corrections for the presence of other particles and particle interactions are also given in literature [23].

2.1.2 Hydrodynamic Interactions

Deposition of Brownian particles onto collector surfaces from flowing suspensions involves two sequential steps: transport and attachment. The transport of the suspended particles toward a stationary surface is dominated by convection and diffusion (the relative importance of each is quantified by the Peclet number which is a measure of convection to diffusion transport). The attachment of these particles is controlled by colloidal forces of interaction, which prevail at shorter separation distances, as well as gravity.

With that in mind, hydrodynamic interactions come into play when examining the convective transport of the particles with the fluid flow. Hydrodynamic forces (or more specifically, drag forces) are exerted by the fluid on the particles due to their relative motion. In the simplest case, the velocity of the suspended particles may be assumed to be the same as the velocity of the fluid which can, in turn, be obtained by solving the Navier-Stokes equation in the absence of the particles. The applicability of this approach is, as expected, limited to dilute suspensions at almost zero particle Reynolds number, where only single- or two-particle interactions prevail. Hence, it is more precise to at least use the *hydrodynamic particle velocity* ($\vec{V}$) instead of the fluid velocity to calculate the drag force, which for the case of a spherical particle in a low Reynolds number fluid flow is given by:

$$F_{Hydro.} = C_f \vec{V} \tag{2.3}$$

As mentioned earlier and will be discussed in Section 2.4.1, correction of the particle velocity and drag force becomes more important for flows close to stationary surfaces [18, 19, 20, 21, 22]. However, incorporation of the long range, many-body hydrodynamic forces between particles in concentrated suspensions remains a long standing problem in statistical mechanics and requires more elaboration [24].

2.1.3 Gravitational Force

The effect of gravitational force is insignificant for Brownian particles (less than 10 μm in size) suspended in a liquid [25]. Gravitational force is more pronounced for cases where the density of the bulk fluid and the suspended particles is very different.

2.1.4 van der Waals Forces

For any pair of fundamental particles (atoms or molecules), among all the possible interactions, interaction energy can arise from:

- Interaction of two non-polar particles, i.e., London-dispersion interactions, which exist between any pair of particles. These interactions arise from the instantaneous dipole moments that occur from electrons orbiting their nuclei.

- Interaction of two rotating permanent dipoles, i.e., Keesom interaction.

- Interaction of a permanent dipole and a non-polar particle, i.e., Debye interaction.

As proposed by London, van der Waals (vdW) interactions comprise all of these interactions, which exhibit decay of interaction potential with $1/r^6$, ignoring the retardation effects (with r being the distance). Obviously, if a permanent dipole does not exist Debye and Keesom interactions do not contribute to the vdW interactions. Otherwise, the contribution of each of the three interactions in the total vdW interaction energy should be considered.

For macroscopic bodies consisting of numbers of atoms or molecules per unit volume, there are two approaches for calculating total vdW potential, both leading to the remarkable conclusion that the interaction energy between macroscopic bodies decays much more slowly with distance ($1/r$ for spheres and $1/r^2$ for flat surfaces versus $1/r^6$ between atoms or molecules). These approaches are listed as follows:

1. Microscopic (Hamaker) Approach: This approach only considers pairwise interactions (i.e., neglects many-body interactions), and assumes that the vdW potential between atoms (or molecules) is additive. This approach is based on summing up all the pair potentials between the individual

atoms (or molecules) in each of the bodies involved. Hamaker used this approach to calculate the interaction between two spheres as well as a sphere and a plane [26]. In the case of the dispersion energy, two atoms in contact have an energy of about $1k_BT$. Hence, the van der Waals potential between macroscopic bodies can be relatively strong compared to thermal energy.

2. Macroscopic Approach: This approach is based on determining the interaction energy by measuring macroscopic properties of materials such as their permittivity and polarizability (or equivalently, refractive index). The macroscopic approach yields the same power-law dependency and Hamaker constant values as the microscopic approach. While Lifshitz was the first to use this approach [27], several developments to his first work were made afterwards [28, 29].

Pursuing the case of macroscopic bodies further, the van der Waals potential is always attractive in vacuum, but in another medium, it can be repulsive. The van der Waals potential only depends on fixed system properties such as Hamaker constant and particle size (Hamaker constant is within $1k_BT_{room}$ to $100k_BT_{room}$ for most materials interacting in vacuum and lower for non-vacuum media).

2.1.5 Electrostatic Forces

Electrostatic interactions exist due the presence of charges on the particles. They arise from Coulombic interactions between electrically charged species. For macroscopic bodies suspended in a bulk fluid, the surface charge of the bodies creates an electrostatic field which subsequently affects the ions in the bulk of the fluid and leads to the formation of electric double layers (EDLs). Zeta potential is then used for estimating the EDL charge. The characteristic thickness of the EDL is the Debye length, κ^{-1}. In aqueous solutions, the thickness is typically on the scale of a few nanometers and it decreases with increasing concentration of the electrolyte in the bulk. κ^{-1} is the distance at which the attraction force from the charged surface on the counter-ions in the bulk fluid is balanced/compensated with diffusion [30].

As mentioned earlier in Section 2.1.4, one characteristic of the vdW potential is that it decays with the distance between the particle and the collector. EDL potential, on the other hand, exhibits an exponential decay behavior with the distance between the particle and the collector, which is influenced by the Debye length. EDL potential varies depending on the pH of the solution which in turn affects the surface electric potential and surface charge of the particles.

2.2 Modeling the Deposition of Ceria on Silica

2.2.1 Multilayer Deposition Model

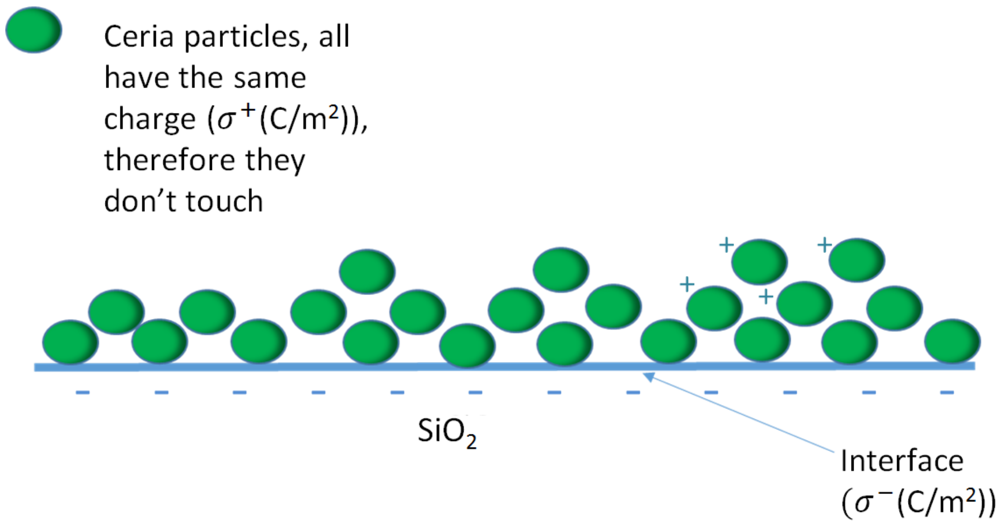

Figure 2.1: Illustration of the multilayer deposition of ceria particles on silica surface.

Multilayer deposition (shown in Figure 2.1) is a possible model to describe dynamics of interaction of ceria nanoparticles with silica surface. Few approaches exist in literature to describe a multilayer deposition process [31, 32, 33]. A simplified approach for describing 2-dimensional multilayer deposition of particles on an oppositely charged surface is inspired by the seminal work of Madelung [34, 35] who described the crystal structure of solid state materials by means of a simple, intuitive approach. In order to investigate the formation of mulilayers of ceria particles on an oppositely charged silica surface, several interactions should be taken into account, including the repulsive energy between ceria particles within each layer, the repulsive energy between ceria particles in the subsequent layers, and the attractive energy between ceria particles and silica surface. Although the exact electrostatic energy between the layers depends on the configuration of each layer with respect to the others, one simple way of looking at the dynamics of the process is the way we look at a clean sensor surface during the formation of a monolayer, that is, as ceria particles approach a partially coated surface *all the NET charge on the sensor surface is felt*, *by equal weight*, by each ceria particle. Therefore, instead of considering a repulsion between the approaching ceria particles and deposited ceria particles, the approaching particles feel an attraction to a surface with *less opposite charge* than the original clean sensor.

2.2.2 Monolayer Deposition Model

To describe dynamics of interaction of ceria nanoparticles with silica surface, deposition of a monolayer (i.e., taking into account only the first ceria layer in the multilayer model) is sufficient. Since such model has the advantage of being much simpler than the multilayer deposition scenario, it is examined in more detail here. It is assumed that the bulk concentration of the particles is sufficiently low to ignore particle-particle interactions and only consider particle-collector interactions. Before delving into the problem, the next section describes DLVO and XDLVO theories, as foundations for in-depth investigation of the monolayer deposition model.

2.3 Interaction Energy Study (Analysis of Monolayer Deposition)

2.3.1 DLVO Interaction Energy Analysis

A common approach for explaining the experimentally observed behavior of colloidal particles at the initial stages of particle aggregation or deposition is the determination of the interaction energy in the framework of DLVO theory. In this framework, the behavior of the system depends on the balance between electrostatic interactions (i.e., electric double layer (EDL) interactions) and London-van der Waals interactions. The former can be obtained by solving the Poisson-Boltzmann (PB) equation [36, 37, 38] and the latter can be obtained using Hamaker's integration approach [37, 38, 26]. One can use well-known approximate analytical formulas for EDL and vdW interaction energies in the case of the interaction of a flat plate (denoted by c, standing for collector) and a spherical particle (denoted by p) to obtain the total interaction energy as:

$$U_{DLVO} = U_{EDL} + U_{vdW} \tag{2.4}$$

U_{EDL} is obtained based on the analytical solution of the linearized PB equation for the case of two infinite planar surfaces by assuming constant surface potential [39] as the boundary condition and then modifying the result based on Derjaguin's approximation [40] for the geometry of a sphere interacting with a planar surface:

$$U_{EDL} = \pi\epsilon_0\epsilon_r a_p[\psi_p^2 + \psi_c^2]\left[\frac{2\psi_p\psi_c}{\psi_p^2 + \psi_c^2}\ln\left(\frac{1+e^{-\kappa d}}{1-e^{-\kappa d}}\right) + \ln(1-e^{-2\kappa d})\right] \tag{2.5}$$

where ϵ_0 is the dielectric permittivity of vacuum, ϵ_r is the relative permittivity of the electrolyte (i.e., water), a_p is the radius of the particles, ψ_p is the surface potential of the particles, ψ_c is the surface potential of the sensor surface, κ is the inverse Debye screening length, and d is the distance of closest approach between the particles and the sensor surface, all in their corresponding SI units.

U_{vdW} is obtained by starting from non-retarded vdW interaction energy for the case of two infinite planar surfaces (based on Hamaker's approach) and then modifying the result based on either Derjaguin's approximation or Surface Element Integration (SEI) approach [41] for the geometry of a sphere interacting with a planar surface:

$$U_{vdW} = -\frac{A_H}{6}\left[\frac{a_p}{d} + \frac{a_p}{d + a_p} + \ln\left(\frac{d}{d + 2a_p}\right)\right] \simeq -\frac{A_H}{6}\left[\frac{a_p}{d}\right] \tag{2.6}$$

where A_H is the effective Hamaker constant of the interacting materials.

To estimate the DLVO interaction energy theoretically, numerical values for the required parameters should be determined experimentally. The numerical values for surface potential of ceria particles and silica-coated sensor were either measured experimentally or taken from literature [1], primary particle size obtained from DLS measurements was used as the size of ceria particles (this is due to the fact that majority of nanoparticles in the suspension have the primary size and the population of aggregates in the suspension is relatively low (see Section 4.1.1 for details)). The effective Hamaker constant was calculated based on the values reported in literature [42, 43]. Debye screening length was calculated based on the value reported by the ceria supplier for the concentration of acetate counter-ions in the ceria slurry (see Table 3.1).

Although DLVO theory is widely used to investigate interaction energy variations as the colloidal particles approach the surface, it fails to predict the behavior of the systems in which hydrogen and chemical bonds are involved in the interactions. This is due to the fact that in DLVO theory, both the surface and the particles are assumed to be chemically inert. Therefore, improvements to the classical DLVO theory have been made to account for additional interactions and explain, where applicable, the discrepancies between experimental observations and predictions of this theory.

Figure 2.2 illustrates the dimensionless total interaction energy curves (i.e., the total interaction energy normalized by the thermal energy of the system) obtained from the summation of attractive vdW potential and electrostatic potential under three different pH conditions: pH 3 and 7 as representatives of favorable conditions for the attachment of ceria to silica (At pH 3 and 7, ceria particles are positively charged and the silica sensor bears a negative charge.), and pH 10 as representative of an unfavorable condition (At pH 10, both the particles and the sensor bear a negative charge.). These graphs will be discussed in more detail in Chapter 4, Section 4.3.2. The corresponding MATLAB codes for calculating DLVO interaction energies are given in Appendix A.

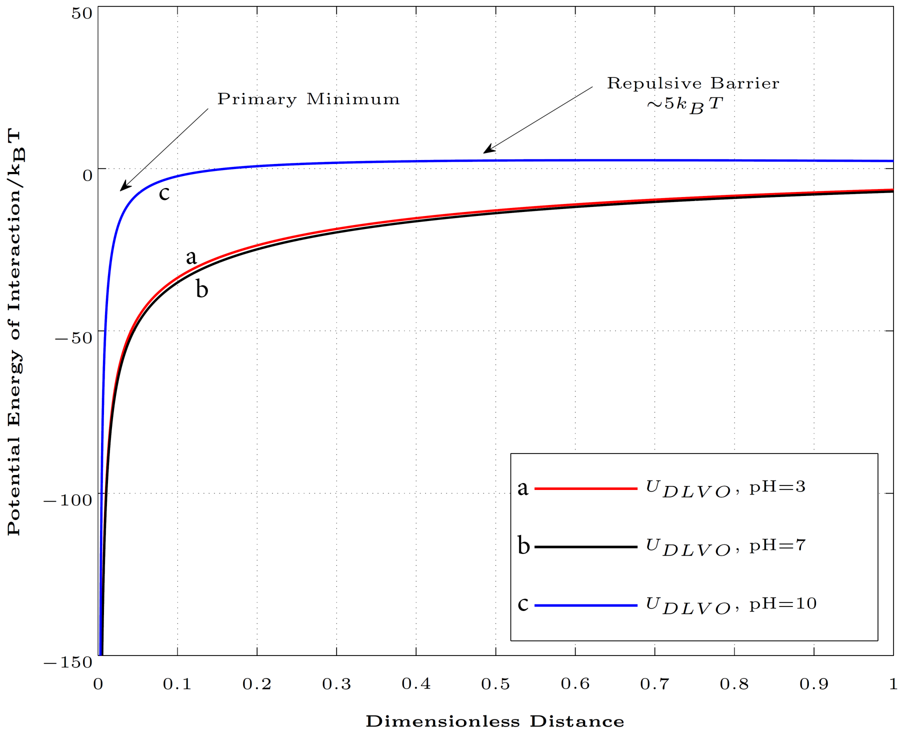

Figure 2.2: Effect of pH on DLVO interaction energy for a ceria nanoparticle approaching a flat silica surface. Abscissa is the dimensionless separation distance (i.e., the distance of closest approach between the particle and the sensor surface normalized by the diameter of the particle) between the spherical particle and the sensor.

According to Figure 2.2, at pH 10, where both the particles and the sensor are negatively charged, the electrostatic repulsive potential forms a moderate repulsive barrier $\sim 5k_BT$ (with k_B being the Boltzmann constant) which prevents the particles from approaching the sensor, yielding to zero deposition. As the pH is decreased, the surface charge of the particles becomes positive and the electrostatic force changes from repulsion to attraction. Subsequently, the particles can get sufficiently close for vdW forces to act and promote the capture of nanoparticles by the sensor in the primary minimum. This is confirmed by the experimentally obtained deposition rates which will be discussed in Section 4.3.2.

2.3.2 XDLVO Interaction Energy Analysis

It has been suggested by van Oss [44, 45] that the total interaction energy between two entities immersed in a polar medium (such as water) has contributions not only from EDL and vdW interactions but also from so called acid-base (AB) interactions. AB interactions are short range interactions, either attractive (known as hydrophobic attraction) or repulsive (known as hydrophilic repulsion), that can be orders of magnitude greater than EDL and vdW interactions [46]. AB interactions include in themselves osmotic pressure, steric interactions, depletion interactions, hydrogen bonding, π-electron bonding, and electron acceptor/electron donor interactions. One can use well-known analytical formulas for AB interaction energies in the case of the interaction of a flat plate and a spherical particle to obtain the total interaction energy in the framework of XDLVO theory as:

$$U_{XDLVO} = U_{EDL} + U_{vdW} + U_{AB} \tag{2.7}$$

U_{EDL} and U_{vdW} are obtained as mentioned in Section 2.3.1. U_{AB} is obtained starting from the AB interaction energy for the case of two flat parallel plates and then modifying the result based on Derjaguin's approximation for the geometry of a sphere interacting with a planar surface. Details for obtaining U_{AB} have been well-described elsewhere [47], leading to the following equation for the geometry of a sphere interacting with a planar surface:

$$U_{AB} = 8\pi a_p \lambda \Delta U_{AB,d_0} e^{\frac{d_0 - d}{\lambda}} \tag{2.8}$$

where $\Delta U_{AB,d_0}$ is the hydration interaction energy at contact which is obtained from the interfacial tension between the interacting materials and the solvent. λ is the characteristic decay length of AB interactions in the solvent and common practice is to take it as 0.6 nm (can be taken from 0.6 to 1.0 nm) for water. d_0 is a cut-off distance due to the repulsion arising from the overlap of the electron clouds of non-covalently bounded interacting atoms; where common practice is to take it as 0.158 nm (can be taken from 0.1 to 0.3 nm).

$$\begin{aligned} \Delta U_{AB,d_0} = {} & 2\sqrt{\gamma_l^+}\left(\sqrt{\gamma_c^-} + \sqrt{\gamma_p^-} - \sqrt{\gamma_l^-}\right) \\ & + 2\sqrt{\gamma_l^-}\left(\sqrt{\gamma_c^+} + \sqrt{\gamma_p^+} - \sqrt{\gamma_l^+}\right) \\ & - 2\left(\sqrt{\gamma_c^+\gamma_p^-} + \sqrt{\gamma_c^-\gamma_p^+}\right) \end{aligned} \tag{2.9}$$

where γ^+ and γ^- are surface tension components of ceria particles (subscript p), silica surface (subscript c), and water as the solvent (subscript l), which can be determined by contact angle measurements [45, 47]. γ^+ and γ^- are related to the material's ability to accept and donate electrons, respectively.

The numerical values for surface tension components of silica and water were taken from reference [48], the corresponding values for ceria were taken from reference [17]. These values are summarized in Table 2.1. According to the existing literature, in numerous cases, the XDLVO approach provides improved qualitative and quantitative predictions compared to other approaches (such as DLVO and surface thermodynamics approach) and methods (such as AFM force measurements). This is true for several particle-surface and particle-particle combinations [17, 47, 49, 50], but is not necessarily the case for all systems. In particular, in case of solids, the evaluation of surface free energy is less straight forward than liquids as it is strongly affected by the kind of chemical bonds that hold a crystal together [51]. In addition, the presence of surface active counter-ions can make the experimentally observed behavior of the systems more difficult to predict [51].

Table 2.1: Surface free energy components for ceria, silica and water used in XDLVO interaction energy study

	γ^+ (mJ/m^2)	γ^- (mJ/m^2)
Ceria	0.21	67.73
Silica	0.8	41.4
Water	25.5	25.5

In light of the fact that the DLVO theory predicts a relatively small repulsive energy barrier at pH 10 (see Figure 2.2), the XDLVO theory was also utilized in this work to predict the behavior of the system under the aforementioned pH conditions and the results are presented in Figure 2.3. The corresponding MATLAB codes are given in Appendix A. Evidently, the XDLVO theory predicts extremely large repulsive hills. In other words, the XDLVO energy profile predicts that attachment is unfavorable under all pH conditions studied here. We will see in Section 4.3.2 that this is not consistent with the behavior of the experimental system. Therefore, although the XDLVO theory is extremely useful in reconciling experimental results with the DLVO approach in numerous cases, the important observation here is that it fails to provide improved insight to the interaction of ceria and silica. For this reason, AB interactions will not be taken into account for the rest of our discussion.

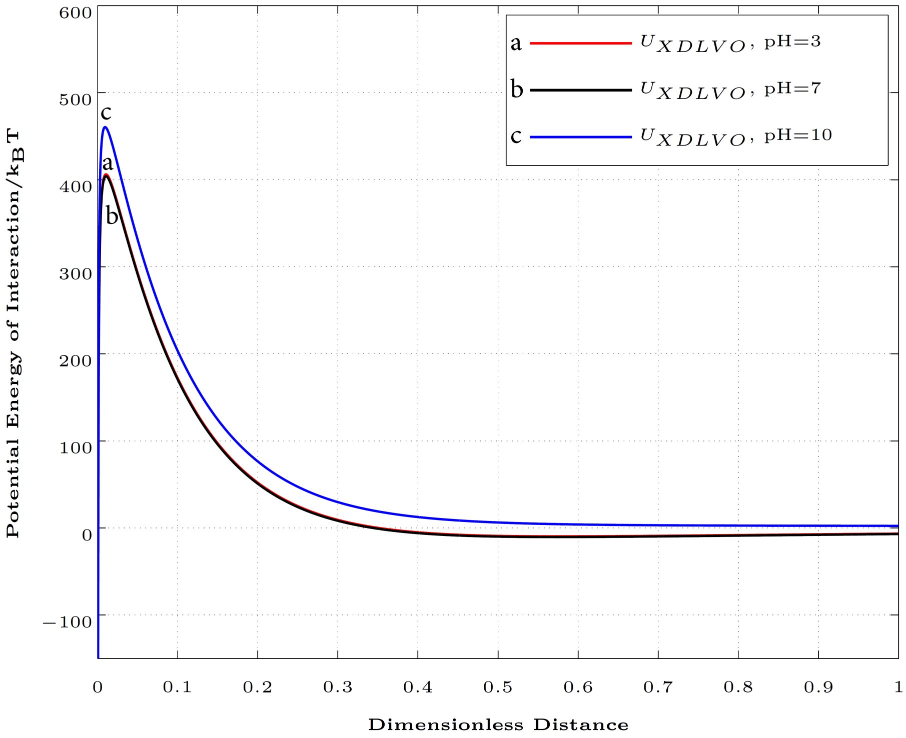

Figure 2.3: Effect of pH on XDLVO interaction energy for a ceria nanoparticle approaching a flat silica surface. Abscissa is the dimensionless separation distance (i.e., the distance of closest approach between the particle and the sensor surface normalized by the diameter of the particle) between the spherical particle and the sensor.

2.4 Governing Transport Model

A 2-D mathematical model is used to describe particle transport in our system. The model incorporates both hydrodynamic and colloidal interactions to predict the initial deposition behavior. This section briefly describes some of the key features of this theoretical model and certain modifications that address its applicability to the QCM-D setup as a system with planar collector geometry. In addition, a simple kinetic equation is proposed to extract initial deposition rates from experimentally obtained QCM-D data. Using the experimentally measured parameters of the system such as particle charge and size, the model was numerically solved and its ability to explain the experimental data was assessed.

2.4.1 Mathematical Formulation and Numerical Solution of the Governing Transport Model

As mentioned earlier, deposition of flowing colloidal particles on a stationary, large collector (sensor) surface occurs due the combination of Brownian motion, hydrodynamic interactions, gravitational forces, van der Waals forces, and electrostatic forces. One way to study this phenomenon is to study the distribution of particles in space, i.e., the Eulerian approach. One can start from the well-known convection-diffusion-migration equation to study the particle deposition phenomena:

$$\frac{\partial n}{\partial t} + \nabla.\vec{j} = Q \tag{2.10}$$

where n is the number concentration of the particles, t is time, $\vec{j}$ is flux of the particles (in $\#/\mathrm{m}^2.\mathrm{s}$) and Q is the source term. The aforementioned interactions are included in the flux term ($\vec{j}$) as follows:

$$\vec{j} = \vec{V}n - \bar{\bar{D}}.\nabla n + \frac{n}{k_B T}\bar{\bar{D}}.\vec{F} \tag{2.11}$$

where $\vec{V}$ is the particle velocity, $\bar{\bar{D}}$ is the diffusion coefficient tensor, and $\vec{F}$ includes all the field forces (i.e., vdW, EDL, gravity). Meanwhile, $\bar{\bar{D}} = \begin{bmatrix} D_{xx} & D_{xz} = 0 \\ D_{zx} = 0 & D_{zz} \end{bmatrix}$ and $\vec{F} = \begin{bmatrix} F_x \\ F_z \end{bmatrix}$.

Considering the system in Cartesian coordinates (see Figure 2.4), Equation 2.11 becomes (assuming symmetry in y-direction):

$$j_x = V_x n - (D_{xx}\frac{\partial n}{\partial x}) + \frac{n}{k_B T} D_{xx} F_x \tag{2.12}$$

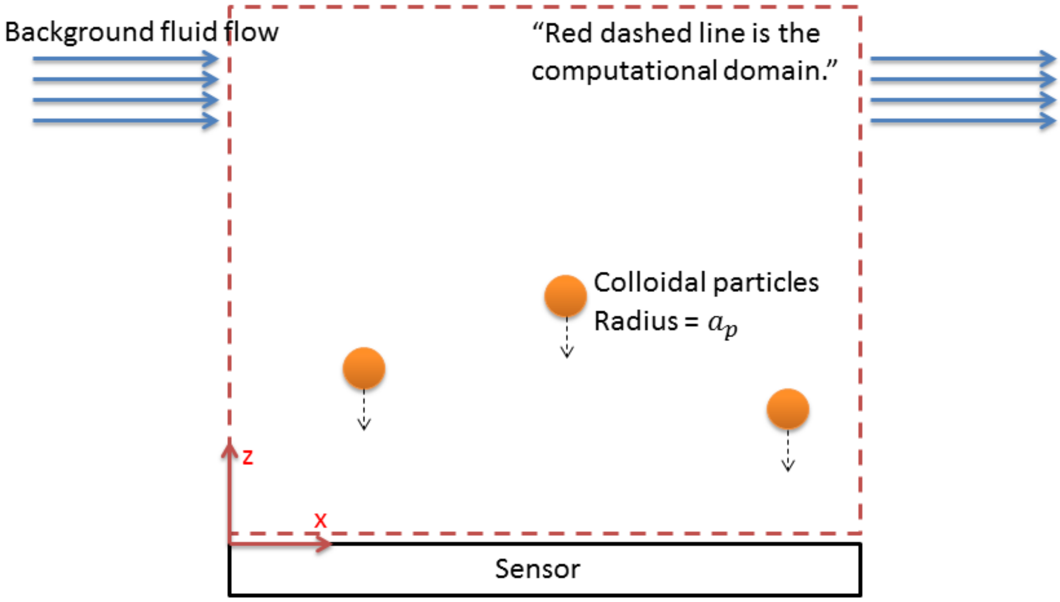

Figure 2.4: Schematic representation of the domain over which the governing transport equations are solved (not drawn to scale).

$$j_z = V_z n - (D_{zz}\frac{\partial n}{\partial z}) + \frac{n}{k_B T} D_{zz} F_z \tag{2.13}$$

Hence, one needs to:

1. Relate fluid velocity ($\vec{u}$) to particle velocity ($\vec{V}$);
2. Relate D_{xx} and D_{zz} to D_∞, which can then be obtained from the Stokes-Einstein relationship.

To this end, Spielman and Fitzpatrick [22] took the deviation from both the Stokes flow and the Stokes-Einstein equation due to the presence of a collector into account. They used *universal hydrodynamic functions* to correct the diffusion and particle motion for a spherical particle near a flat solid surface, denoted by $f_1(h)$ to $f_4(h)$, as a function of the dimensionless distance ($h = \frac{z}{a_p} - 1 = \frac{d}{a_p}$) of the form:

$$f_i = 1 + b_i exp(-c_i h) + d_i exp(-e_i h^{a_i}) \tag{2.14}$$

where i varies from 1 to 4. The variation of these functions with the dimensionless distance h is shown in Figure 2.5.

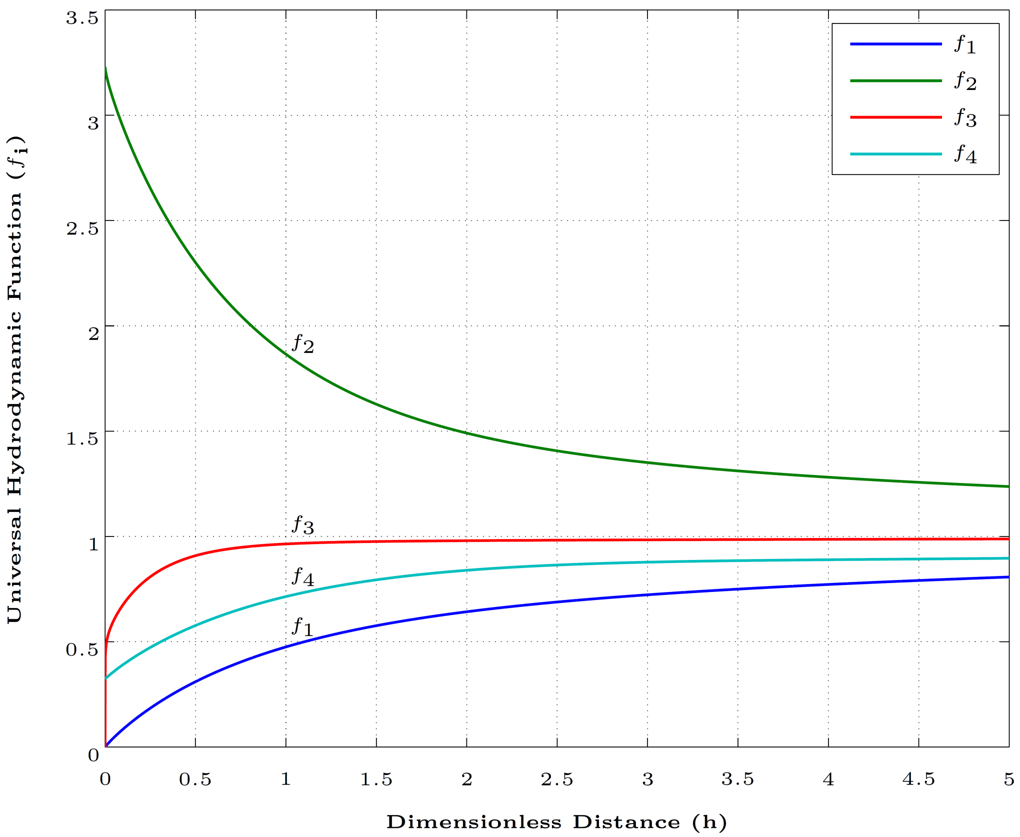

Figure 2.5: Universal hydrodynamic correction functions (f_i) for a spherical particle near a plane. Abscissa is the distance of closest approach normalized by the radius of the particle.

Following their work:

$$V_x = u_x f_3(h) \tag{2.15}$$

$$V_z = u_z f_1(h) f_2(h) \tag{2.16}$$

And, also:

$$D_{xx} = D_\infty f_4(h) \tag{2.17}$$

$$D_{zz} = D_{\infty} f_1(h) \tag{2.18}$$

Therefore, one can substitute all of these parameters in j_x and j_z (equations 2.12 and 2.13):

$$j_x = u_x f_3 n - (D_{\infty} f_4 \frac{\partial n}{\partial x}) + \frac{n}{k_B T} D_{\infty} f_4 F_x \tag{2.19}$$

$$j_z = u_z f_1 f_2 n - (D_{\infty} f_1 \frac{\partial n}{\partial z}) + \frac{n}{k_B T} D_{\infty} f_1 F_z \tag{2.20}$$

Referring back to equation 2.10, at steady state and in the absence of the source term, this equation simplifies to:

$$\nabla . \vec{j} = 0 \tag{2.21}$$

which is equivalent to:

$$\frac{\partial j_x}{\partial x} + \frac{\partial j_z}{\partial z} = 0 \tag{2.22}$$

which after substituting j_x and j_z from above, leads to:

$$\begin{aligned} &\frac{\partial}{\partial x}\left(u_x f_3 n - (D_{\infty} f_4 \frac{\partial n}{\partial x}) + \frac{n}{k_B T} D_{\infty} f_4 F_x\right) \\ +&\frac{\partial}{\partial z}\left(u_z f_1 f_2 n - (D_{\infty} f_1 \frac{\partial n}{\partial z}) + \frac{n}{k_B T} D_{\infty} f_1 F_z\right) = 0 \end{aligned} \tag{2.23}$$

The next step is to simplify this equation for the setup at hand. According to the background fluid flow in our system, $u_z = 0$. In addition, u_x is assumed to be constant and can be obtained from the experimental conditions (i.e., using the flow rate and QCM-D chamber dimensions). Lastly, it is assumed that in our system, $F_x = 0$ and F_z has contributions from gravity, vdW and EDL forces which need to be specified one by one:

- Gravitational force:

$$F_{z,g} = -\frac{4}{3}\pi a_p^3 \Delta\rho g \tag{2.24}$$

where $\Delta\rho$ is the difference between density of the particle and the fluid.

- van der Waals force:

$$F_{z,vdW} = -\frac{A_H}{6}\frac{1}{a_p h^2} \tag{2.25}$$

where A_H is the effective Hamaker constant (i.e., A_{123}).

- Electrostatic (EDL) force:

$$F_{z,EDL} = \pi\epsilon_0\epsilon_r a_p[\psi_p^2 + \psi_c^2]\left[\frac{2\kappa exp(-\kappa a_p h)}{1 - exp(-2\kappa a_p h)}\right]\left[\frac{2\psi_p\psi_c}{\psi_p^2 + \psi_c^2} - exp(-\kappa a_p h)\right] \tag{2.26}$$

where in deriving the equation, constant surface potential was assumed as the particles approach the sensor.

Finally, we just need to substitute everything into Equation 2.23 and solve (numerically) for n (more precisely, for $n(x, z)$) subject to appropriate boundary conditions. This allows for the calculation of j_z which can subsequently be integrated over a surface (more precisely, a line, as symmetry in y-direction was assumed) parallel to the sensor to give the rate of deposition of particles.

The following boundary conditions are used:

- $z = 0$, $n = 0$;

  Note: As $F_{z,vdW}$ diverges at $z = 0$, this boundary condition was actually applied at $z = \delta$ (such that $\frac{\delta}{a_p} = 10^{-4}$).

- $z = chamberheight$, $\vec{j} = 0$ (Zero flux or wall boundary condition);

- $x = 0$, $n = n_{bulk}$;

- $x = sensordiameter$, $i.\nabla n = 0$ (Zero dispersive flux in x direction).

As the derivations discussed here are based on the principal assumption that the sensor surface is absolutely clean (note that the values of ψ_p and ψ_c are fixed) and the particles do not accumulate on the sensor surface upon their deposition (note the boundary condition at $z = 0$), this model applies ONLY to the initial stage of the deposition process on a clean sensor. Hence, this model gives an upper bound for the flux of colloidal particles toward the sensor. Nonetheless, as long as one performs the experiments on a clean sensor and calculates initial rate of deposition, the experimental data can be used to validate the model. Otherwise, the model must be modified to account for the sensor surface becoming less favorable for attachment as deposition proceeds.

To numerically solve for concentration distribution and rate of deposition, we take advantage of "coefficient form in PDE mode" in COMSOL Multiphysics software (version 4.3a). The coefficient form, as defined in COMSOL Multiphysics software, has the following format:

$$e_a \frac{\partial^2 n}{\partial t^2} + d_a \frac{\partial n}{\partial n} + \nabla.(-c\nabla n - \alpha n + \gamma) + \beta.\nabla n + an = f \tag{2.27}$$

where all the coefficients are scalars except α, β and γ which are vectors with m components, and also c which can be an $m \times m$ matrix (to model anisotropic properties), and $\nabla = [\frac{\partial}{\partial x}, \frac{\partial}{\partial z}]$. Hence, we can use the following setting to implement our model in COMSOL:

$$\alpha = -\left(\vec{V} + \frac{\bar{\bar{D}}.\vec{F}}{k_B T}\right) = \begin{cases} \alpha_x = -u_x f_3 \\ \alpha_z = -\frac{1}{k_B T} D_\infty f_1 F_z \end{cases} \tag{2.28}$$

$$c = \begin{bmatrix} D_{xx} & D_{xz} = 0 \\ D_{zx} = 0 & D_{zz} \end{bmatrix} = \begin{bmatrix} D_\infty f_4 & 0 \\ 0 & D_\infty f_1 \end{bmatrix} \tag{2.29}$$

And, all the other parameters in Equation 2.27 = 0.

Before proceeding to the solution, it should be noted that for the FEM numerical solver to be able to resolve the concentration gradient near the sensor surface, proper discretization (meshing) of the domain is necessary. The finite element mesh serves two purposes. It first discretizes the geometry into smaller elements, over which it is possible to write a set of equations describing the solution to the governing equation. The mesh is also used to represent the solution field for the system being solved. There is error associated with both the discretization of the geometry as well as discretization of the solution. Hence, although we are always able to compute a solution, no matter how coarse the mesh, but it may not be very accurate. As a general rule for FEM methods, the more elements, the more accurate the solution (that is, the smaller the error). However, even if computational resources are not limited, it is not a good approach to try to have infinitesimal elements because as the individual mesh elements get very small we run into the limits of numerical precision. That is, the numbers in the model become smaller than can be accurately represented on a computer. So, by making the elements smaller and smaller, there is always a point at which the error starts to go back up. As a result, the first thing to do is to perform a mesh refinement study and monitor the convergence of the solution as the mesh is refined. Moreover, the mesh might be refined in an adaptive manner, that is, to make the elements smaller only in regions where the error is high (e.g. near the sensor surface for this system).

The model here was discretized using second-order Lagrangian elements. First, the domain was discretized using an "*extremely fine*" mesh (default in COMSOL) (see figure below) and then, this mesh was adaptively refined (see figure below) to reach an acceptable solution. Adaptive refinement means that the elements were made smaller only in regions where the error is high (i.e., the model was solved on an initial mesh and elements were iteratively inserted into regions where the error is estimated to be high, and then the model was resolved. This procedure continued for 6 to 8 iterations here (depending on the system parameters)).

The solution obtained in this way was used to obtain an estimation of the

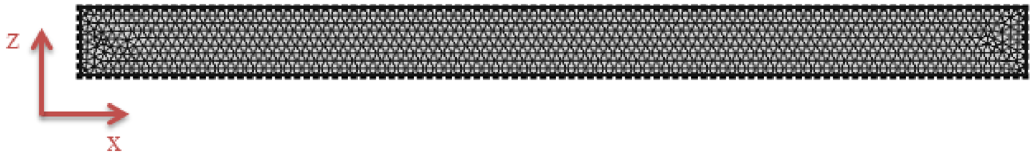

Figure 2.6: Discretization of the computational domain by an "*extremely fine*" mesh (default in COMSOL).

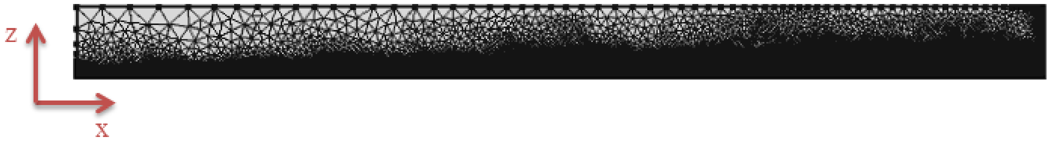

Figure 2.7: Discretization of the computational domain by an adaptively refined mesh (resulting from eight adaptive refinement of the extremely fine mesh).

dimension of the region above the sensor in which considerable concentration gradient exists. It was observed that concentration uniformity is reached within a 2 μm high region along the sensor. In the next step, a boundary layer mesh consisting of 1000 layers with quadrilateral elements was built in the vicinity of the sensor surface which extended to a height of 3 μm above the sensor. This boundary layer mesh was then smoothly joined to the extremely fine triangular mesh to discretize the rest of the domain. A mesh refinement study was also performed and results were compared on different sized meshes. The results obtained based on this custom-generated mesh were confirmed to be independent from the mesh size/number of elements. This mesh guarantees accuracy in resolving the concentration gradient inside the entire domain and, most importantly, the boundary layer along the sensor.

2.4.2 Kinetic Formulation for Raw Experimental Data Fitting

In the case that the simplified monolayer deposition model is valid, using the QCM-D instrument, one can study kinetics of the deposition process as follows.

When the sensor is exposed to a ceria suspension, there is a response from the instrument in the form of frequency or dissipation change. Denoting this response (either f or D) with R, the standard elementary reaction format can be used to describe the rate of change of the response:

$$\frac{dR(t)}{dt} = k_a n_{bulk}(R_{max} - R(t)) - k_d R(t) \tag{2.30}$$

where $R(t)$ is the response corresponding to occupied sites at time t, k_a is the adsorption rate constant, n_{bulk} is the bulk concentration of ceria, R_{max} is the instrument response for the case that all the binding sites on the sensor are occupied by ceria particles, and k_d is the desorption rate constant. Since a reference measurement in the same liquid environment is done prior to each QCM-D experiment (see Section 3.2), the response at the start of the experiment is zero (i.e., $R(t = 0) = 0$). Furthermore, at equilibrium, the response does not change with time (i.e., $\frac{dR(t)}{dt} = 0$). Solving equation 2.30 subject to the aforementioned boundary conditions results in an equation for time evolution of the response:

$$R(t) = R_{eq}\left(1 - e^{-(k_a n_{bulk} + k_d)t}\right) \tag{2.31}$$

or

$$R(t) - R_{eq} = -R_{eq} e^{-(k_a n_{bulk} + k_d)t} \tag{2.32}$$

where R_{eq} is the response at equilibrium. Hence, by doing deposition experiments at different ceria concentrations, an exponential function of the form $y = ae^{bx}$ can be used to fit the time evolution of $R(t)$ in order to obtain adsorption and desorption rate constants for the interaction of ceria particles with silica surface. In addition, the first derivative of this exponential function can be used for interpretation of deposition and release kinetics under different experimental conditions.

Chapter 3

Experimental Procedures

3.1 Sample Preparation

Stock suspension of ceria nanoparticles (Nyacol Nano Technologies) was provided as a stable slurry. The specifications of the stock suspension as provided by the manufacturer are listed in Table 3.1.

Table 3.1: Specifications of ceria slurry used in this study as reported by Nyacol Nano Technologies, Inc.

Ceria content (wt%)	20
Media	water
Primary particle size (nm)	10-20
pH	3.0
Particle charge	positive
Counter-ion (mol/mol)	0.4 acetate
Specific gravity	1.22
Viscosity (cP)	10
Appearance	pale yellow

De-ionized water, prepared by Milli-Q UV PLUS, which is referred to Milli-Q water, was used for slurry dilution and all other occasions as needed. The pH was measured using an Accumet Basic AB15 pH meter, which was calibrated prior to each use. The pH of the samples was adjusted using hydrochloric acid and sodium hydroxide prior to the experiments. All chemicals used to prepare the solutions were of analytical grade.

3.2 QCM-D Experiments

The interaction between colloidal particles is commonly investigated by considering the interplay of several forces of interaction including hydrodynamic forces and non-hydrodynamic forces (e.g. Columbic, van der Waals, Brownian, gravity). QCM-D is indeed an effective tool to study such interactions. Although originally used for investigating biological systems, its use has been extended to the study of many colloidal systems (including NP research). QCM-D technology enables one to track the kinetics, extent and stability of NP interactions as they deposit on surfaces, undergo self-assembly processes, and are utilized to form nanocomposite materials.

QCM technology is based on the oscillation of a quartz crystal (thickness $\sim$300 μm) in a shear-thickness mode at its main resonance frequency and its odd-order overtones. Typically, changes in resonance frequency (Δf) and changes in half band-width at half maximum, or simply changes in band-width ($\Delta\Gamma$) are monitored on several overtones as a film is allowed to form at the surface of the crystal. The Q-sense system used in this study is based on the so called ring-down scheme [52] where the external driving voltage is turned off intermittently to let the oscillations decay freely. Therefore, this system actually measures energy dissipation which is related to band-width as: $D_n = \frac{2\Gamma}{f_n}$, with f_n being the resonance frequency.

In the case of perfectly rigid films ($\Delta D = 0$), well-known Sauerbrey equation [53] can be used to convert Δf_n to mass change (Δm) on the crystal surface. In addition, there exist well-established models based on the propagation of shear waves in viscoelastic media for soft, laterally homogeneous thin films to obtain information such as areal mass density, thickness, viscoelastic properties, and intrinsic structural information by fitting QCM data (Δf_n and ΔD_n) based on a continuum model [54]. However, this approach is not appropriate for investigating the deposition of nanoparticles which form laterally inhomogeneous films (i.e., films consisting of discrete entities) upon attachment to the sensor surface because the film thickness, in our case, is about the same as the length scale of the sample's internal structure (i.e., particle diameter).

Attachment (and release) of ceria nanoparticles onto (and from) a silica surface was examined using a Q-Sense E4 system (Q-sense AB, Gothenburg, Sweden) by simultaneous monitoring of the change in resonance frequency (Δf_n) and dissipation (ΔD_n), with n being the overtone order.

5 MHz silica coated AT-cut quartz crystals (named QSX 303) were mounted in standard flow modules after cleaning (the cleaning procedure is explained below). Before each experiment, the flow modules and tubings were cleaned according to the cleaning protocol suggested by the vendor. Flow modules (as well as all gaskets and o-rings) were first immersed in Milli-Q water and sonicated for 60 minutes. Then, they were rinsed with Milli-Q water and blow-dried with nitrogen gas. The electrodes could not be washed (they are not in direct contact with sample or any other fluid during the experiments) and were kept in a desiccator when not in use. All the tubings were washed by pumping approximately 50 mL of 2 wt% solution of Hellmanex through them, followed by pumping approximately 50 mL of Milli-Q water through them. This was done using the peristaltic pump (ISMATEC IPC-N4) attached to the QCM-D instrument. New sensors were first treated in a UV/ozone chamber (Bioforce Nanosciences, ProCleaner Plus) for 15 minutes. Then, the sensors (as well as the Teflon sensor holder) were immersed in a 2 wt% solution of Sodium Dodecyl Sulfate (SDS) for 30 min at room temperature. After that, the sensors were rinsed thoroughly with Milli-Q water and blow-dried with nitrogen gas. Finally, the sensors were treated in a UV/ozone chamber for another 15 minutes. As the cleaning procedure suggested by the vendor was shown to be ineffective in removing the attached particles from the sensor surface (see Section 4.2),

a modified cleaning protocol was developed to effectively clean the sensors after each experiment. Immediately after each experiment, the sensors were sonicated for 15 minutes in Milli-Q water with pH adjusted to 10 (where the particles and the sensor bear the same (negative) sign of surface charge) to ensure that all the attached ceria particles are released from the sensor surface. This was then followed by the conventional cleaning protocol suggested by the vendor. Prior to each measurement, overtones 1 to 13 were found for the mounted crystal (in some cases overtone 11 was not found). As a quick way to test the accuracy of the QCM-D before each measurement, the frequency measurement of each sensor was verified by monitoring the frequency shift while changing the sensor environment from air to liquid. In air, the frequency of the first overtone should be very close to 5 MHz (4.95 MHz). At the beginning, this value was recorded. Then, the pump, which was connected to Milli-Q water of desired pH, was turned on, changing the sensor environment from air to water. According to the literature [55, 56, 57], the frequency should decrease by ∼721 Hz from the value recorded in air, as the resonance frequency of the sensor depends on the physical properties of the introduced liquid environment as:

$$\Delta f_{air-to-liquid} \propto \sqrt{\rho_{liquid} \cdot \mu_{liquid}} \tag{3.1}$$

where ρ and μ denote density and viscosity, respectively. The frequency shift was verified by this quick test before each measurement.

Stock ceria suspension was diluted to the desired concentration and its pH was adjusted to the desired value before being introduced to the QCM-D instrument (see Section 3.1 for details). Temperature was kept constant at 25 °C during all the measurements. Measurements were performed using silica sensors at four different flow rates (0.05 mL/min, 0.10 mL/min, 0.15 mL/min, and 0.20 mL/min) and seven different concentrations of ceria suspension (0.01 wt%, 0.1 wt%, 0.2 wt%, 0.4 wt%, 0.5 wt%, 0.7 wt%, 1 wt%) at three different pH values (3, 7, 10). Each experiment was repeated at least three times, using independently prepared batches. Data for all overtone frequencies and energy dissipations were collected. However, the 3$^{\text{rd}}$ overtone was used for most data analysis, unless specified otherwise. MATLAB software (MATLAB version R2012b, The MathWorks Inc., Natick, Massachusetts, USA) was used to analyze the raw f and D data points as will be explained later.

3.3 Zetasizer

3.3.1 Sizing

Dynamic Light Scattering (DLS) was used to measure hydrodynamic diameter and particle size distribution (PSD) of ceria particles in the slurry. Measurements were conducted by a Malvern Nano ZS Zetasizer using a folded capillary cell. The stock suspension was diluted to a concentration of 1 wt% to measure PSD (although no difference in the results was observed when performing the measurements using more diluted suspensions). The pH of the suspensions was adjusted prior to the measurements. The measurements were conducted at 25 °C, using a refractive index of 1.330 for water and 2.100 for ceria. Two independently prepared ceria suspensions were used for the measurements and the results reported here are the average of three consecutive measurements on each independent sample. Measurements were also conducted on a Brookhaven ZetaPALS instrument which determines particle size distribution in aqueous media using Phase Analysis Light Scattering (PALS). Phase analysis light scattering produces highly accurate sample measurements versus traditional light scattering methods. Mean diameter and poly-dispersity of ceria particles were obtained by these measurements. These measurements were conducted using disposable clear cuvettes, the same parameters, and the same sample preparation procedure as used in DLS measurements. The results reported here correspond to two consecutive measurements on each independent sample; each repeated ten times and averaged by the instrument using the built-in software.

3.3.2 Electrokinetic Characterization

Laser Doppler velocimetry was used to measure electrophoretic mobility of nanoparticles. Measurements were conducted using a Malvern Nano ZS Zetasizer with a folded capillary cell. The cell was rinsed three times with Milli-Q water and then rinsed three times with the sample suspension prior to each measurement. The initial slurry was diluted to a concentration of 1 wt% for electrophoretic mobility measurement. Two independently prepared ceria suspensions were used for electrophoretic mobility measurements. The pH of the suspensions was adjusted prior to the measurements which were conducted at 25 °C, using a refractive index of 1.330 for water and 2.100 for ceria, dielectric constant of 78.5 for water, and absorptivity of 0.050 for ceria. As the initial ceria suspension was diluted to the concentration of 1 wt% before the measurements, viscosity of the suspension was assumed to be the same as the viscosity of water, 0.8872 cP. Three consecutive measurements were carried out on each independent sample at an applied voltage of ~150 V. Zeta potential of the particles was calculated using Smoluchowski's correlation based on the electrophoertic mobility measurements.

3.4 Imaging

To characterize QCM-D sensor surfaces before and after deposition experiments, Atomic Force Microscopy (AFM) imaging was performed with a Bruker Dimension Edge microscope. The instrument was located on a structurally isolated floor pad in a basement laboratory to minimize vibration. All images were taken using silicon carbide (SiC) cantilevers in tapping mode with phase imaging. In tapping mode, the detector signal is the cantilever oscillation amplitude, that provides 3D topographical information. Phase images were also generated by simultaneously monitoring the phase lag between the periodic signal driving the cantilever and the oscillations of the cantilever. Changes in phase lag indicate changes in the properties of the sample surface that help to map variations in composition. Scans were made on several locations of each sample, from 500 nm to 1 μm in width, and with scan rates of 0.7 Hz to 1 Hz. Nano Drive Dimension Edge software was used to flatten the images. Further image processing was performed by both MATLAB and ImageJ (National Institutes of Health, Bethesda, Maryland, USA) software (see Appendix B for details).

Scanning Electron Microscopy (SEM) was also used to characterize the deposited particles on QCM-D sensors. The SEM measurements were carried out using a JAMP-9500F Auger microprobe (JEOL) at the Alberta Center for Surface Engineering and Science, University of Alberta. The instrument is equipped with Shottky field emitter that produces an electron probe diameter of ∼3 to 8 nm on the sample. The accelerating voltage and emission current for the SEM imaging were set at 15 kV and 8 nA, respectively. The working distance was 23 to 24 mm. The sample was rotated 30 degrees away from the primary electron beam to face the electron energy analyzer. Since both the silica coated sensor surface and deposited ceria NPs are nonconductive, prior to the SEM measurements, the samples were coated with an ultrathin coating of chromium to avoid image faults and artifacts due to build-up of electrostatic charge while being scanned with the electron beam.

Chapter 4

Results and Discussions

4.1 Characterization of Nanoparticles

4.1.1 Sizing

Depending on their preparation methods, colloidal nanopaticles exhibit particle distinct size distribution, as opposed to being monodispersed. As the size of the nanoparticles is known to affect their aggregation and deposition, it is important to determine their particle size distribution. Table 4.1 summarizes the results of particle size measurements by both DLS and PALS techniques at pH 3. Although only a single average hydrodynamic diameter is reported by either DLS or PALS measurements, there are a number of peaks in intensity-size graphs that represent more accurate information on the actual size distribution of the particles in the slurry. According to the intensity-size graphs, three peaks are easily distinguished, which correspond to the size of the primary nanoparticles, growing (or moderate-size) nanoparticle aggregates, and large nanoparticle aggregates, respectively. Considering the corresponding number-size graphs (see Appendix C for details), one can conclude that majority of nanoparticles in the suspension have the primary size and the population of aggregates in the suspension is relatively low. Hence, ceria particles used in

Table 4.1: Specifications of ceria particles used in this study as measured by DLS and PALS

Measured parameter	DLS	PALS
Ceria content (wt%)	1	1
Media	water	water
pH	3.0	3.0
Primary particle size (hydrodynamic diameter) (nm)	5.86	4.50
Average particle size (hydrodynamic diameter) (nm)	21.24	27.45
Polydispersity index	∼0.4	0.223
Zeta Potential (mV)	51.25	N/A

this study can be well characterized by a single size (in other words, their polydispersity index (PDI) is relatively low). The results are in agreement with the particle size provided by the supplier (see Table 3.1). This result is also expected from the the results of zeta potential measurements (see Section 4.1.2 or Table 4.1). At pH 3, average zeta potential of ceria nanoparticles is 51.25 mV. Under this condition, the electrostatic (repulsion) interactions are dominant and prevent the particles from forming aggregates. Another investigation of the same ceria particles under similar conditions reported similar results [1].

4.1.2 Electrokinetic Characterization

Electrophoretic mobility of ceria nanoparticles was measured and converted to zeta potential according to Smoluchowski's correlation. The results measured at pH 3 are summarized in Table 4.1. In another study [1], electrophoretic mobility of the same ceria nanoparticles, as well as silica nanoparticles, was evaluated over a wide range of pHs. According to that study, the isoelectric point or point of zero charge for ceria is at pH ∼9 where the zeta potential of the particles changes from positive to negative by increasing the pH. Silica is negatively charged over the entire pH range of 3 to 11 [1].

In this study, we investigate the deposition behavior of ceria particles onto silica surface at three pH values which represent both favorable and unfavorable deposition conditions. Pursuing this further, we referred to a previous study done by Lin et al. [1] who measured the zeta potential of silica and ceria over a wide range of pHs (their results are presented in Figure 4.1). As illustrated in Figure 4.2, investigation of Figure 4.1 reveals embedded information on the stability of ceria slurry at different pHs and determines regions of favorability of the attachment of ceria and silica.

4.2 Optimization of QCM-D Cleaning Procedures and Experimental Conditions

QCM-D sensors (collectors) are usually cleaned and used a few times in real world experimental work. Sensor cleaning procedures that are used today were initially developed based on biological applications. Thus, one needs to make sure that these procedures are suitable when working with other systems; especially the systems in which charged moieties are studied and hence electrostatic interactions inevitably have to be taken into account, to make sure that the sensors, after cleaning, act as new ones and the results are reliable. This issue will be addressed here, as it was one of the early obstacles encountered in this work.

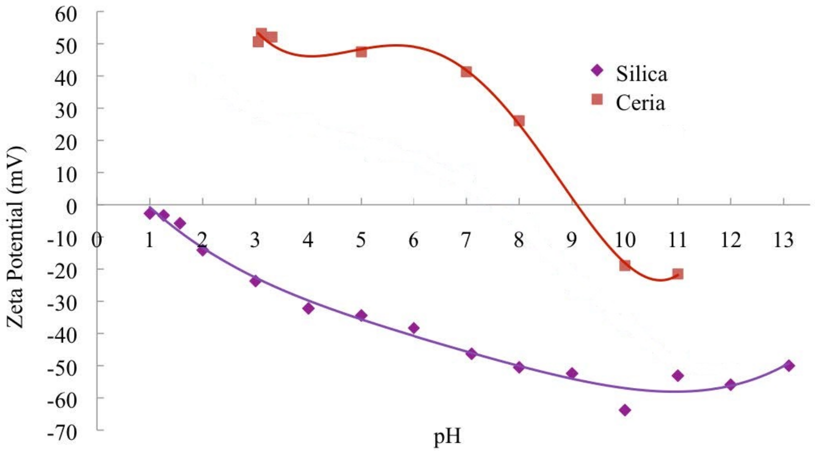

Figure 4.1: Zeta potential of silica and ceria as a function of pH, reproduced by permission of The Electrochemical Society [1].

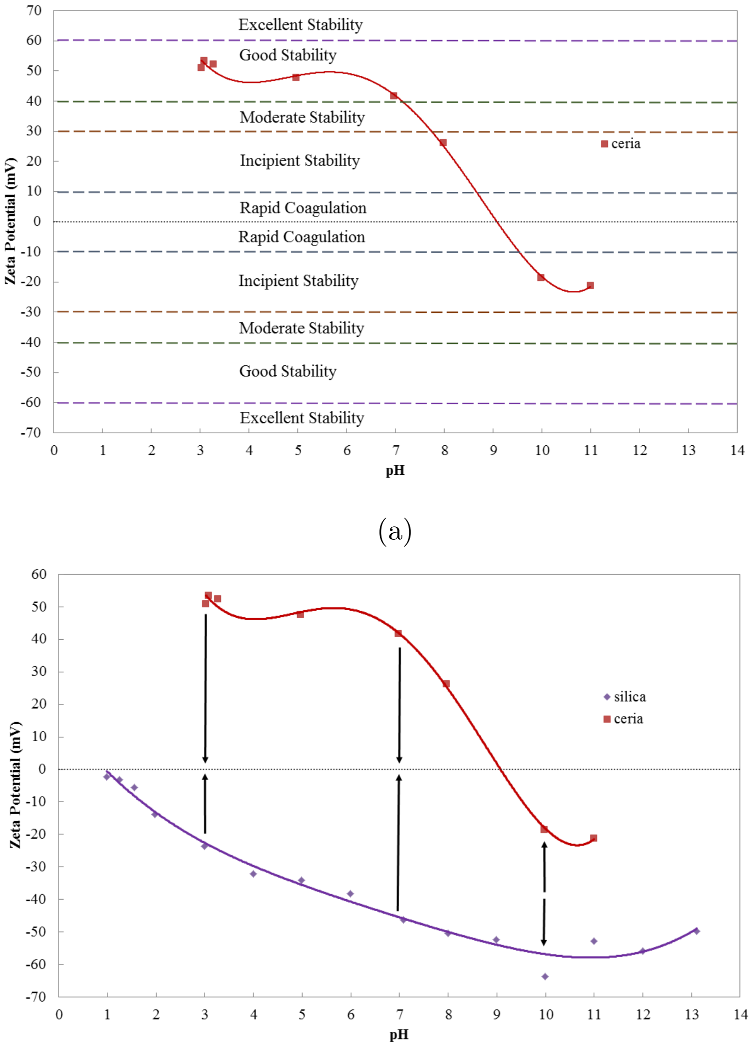

(a)

(b)

Figure 4.2: Plots of zeta potential vs pH for silica and ceria showing (a) regions of different degrees of stability of their slurries, and (b) different states of favorability of their attachment (arrows at pH 3 and 7 indicate attachment of the two substances while arrows at pH 10 indicate repulsion).

It is well-known that as a collector surface is covered by deposited particles its capture efficiency changes. This change can have a major outcome: it can prevent or hinder the deposition of the subsequent particles (known as "blocking"). It is discernible that blocking is caused by:

1. reducing the number of available surface sites for attachment (known as

"steric hindrance");

2. rendering the collector surface less attractive or less favorable for attachment (known as "electrostatic hindrance").

In spite of its tremendous consequences, blocking of the collector (sensor) surface by previously-deposited particles has received considerably less attention in developing and/or improving the cleaning procedures when extending the use of QCM-D sensors in studying colloidal interactions. When a film is allowed to deposit on the surface of a new sensor, some particles are attracted to the sensor surface and bond to this surface in an "irreversible" manner while some particles deposit in a "reversible" manner. The ones that are reversibly attached will be released/detached in the rinsing step (a microscopic graph taken after this step can easily show the extent of the surface coverage and determine the occurrence of a monolayer versus multilayer deposition).

According to Figure 4.3, as particles are deposited on new sensors, the new sensors appear to have a bimodal frequency shift, that is, there is a stage with a steep slope (which corresponds to the irreversibly-attached particles) followed by a stage with moderate slope (which corresponds to the reversibly-attached particles which can be washed off during the rinsing step). New sensors give consistent results in this regard. Our results (both QCM-D and micrographs) illustrate that under favorable attachment conditions, a considerable amount of particles are irreversibly attached to the sensor surface, leading to a net frequency shift (see Figures 4.3 and 4.4 as an example).

The conventional cleaning protocols differ from each other, depending on the sensor type. In other words, the nature of the sample introduced to the sensor is ignored in determining the proper cleaning procedure. Conventional cleaning protocol suggested by Q-sense for silica coated sensors (referred to as *Cleaning Protocol B-I*) is briefly shown in Figure 4.5a. As will be discussed in this chapter, we have modified this protocol (Figure 4.5b) to ensure an effec-

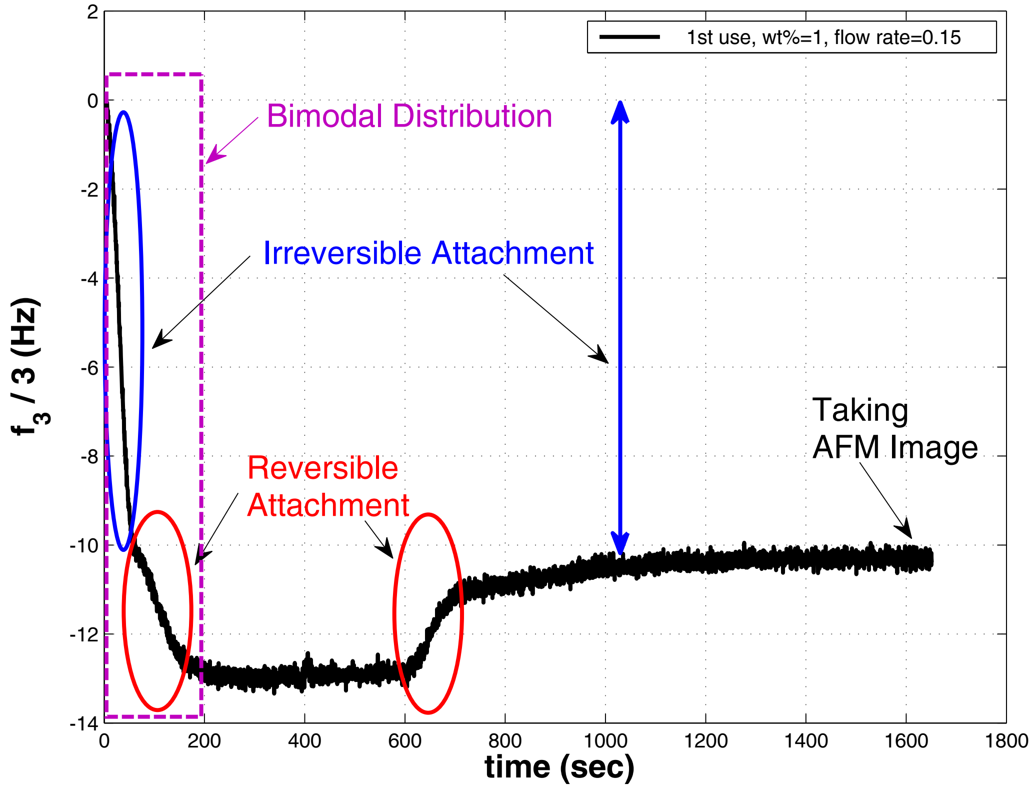

Figure 4.3: Frequency shift due to particle deposition on a new sensor showing the extent of reversible and irreversible attachment.

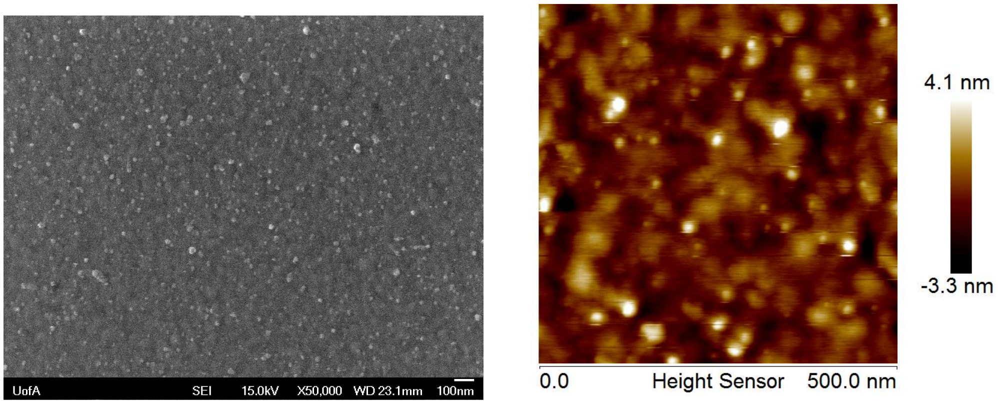

(a)

(b)

Figure 4.4: SEM (a) and AFM (b) images taken at the end of an experiment (after rinsing off the reversibly attached particles), showing the particles that are irreversibly attached onto a new sensor.

tive sensor cleaning after the experiments. Performing conventional cleaning procedure between identical experiments, results in several notable changes in

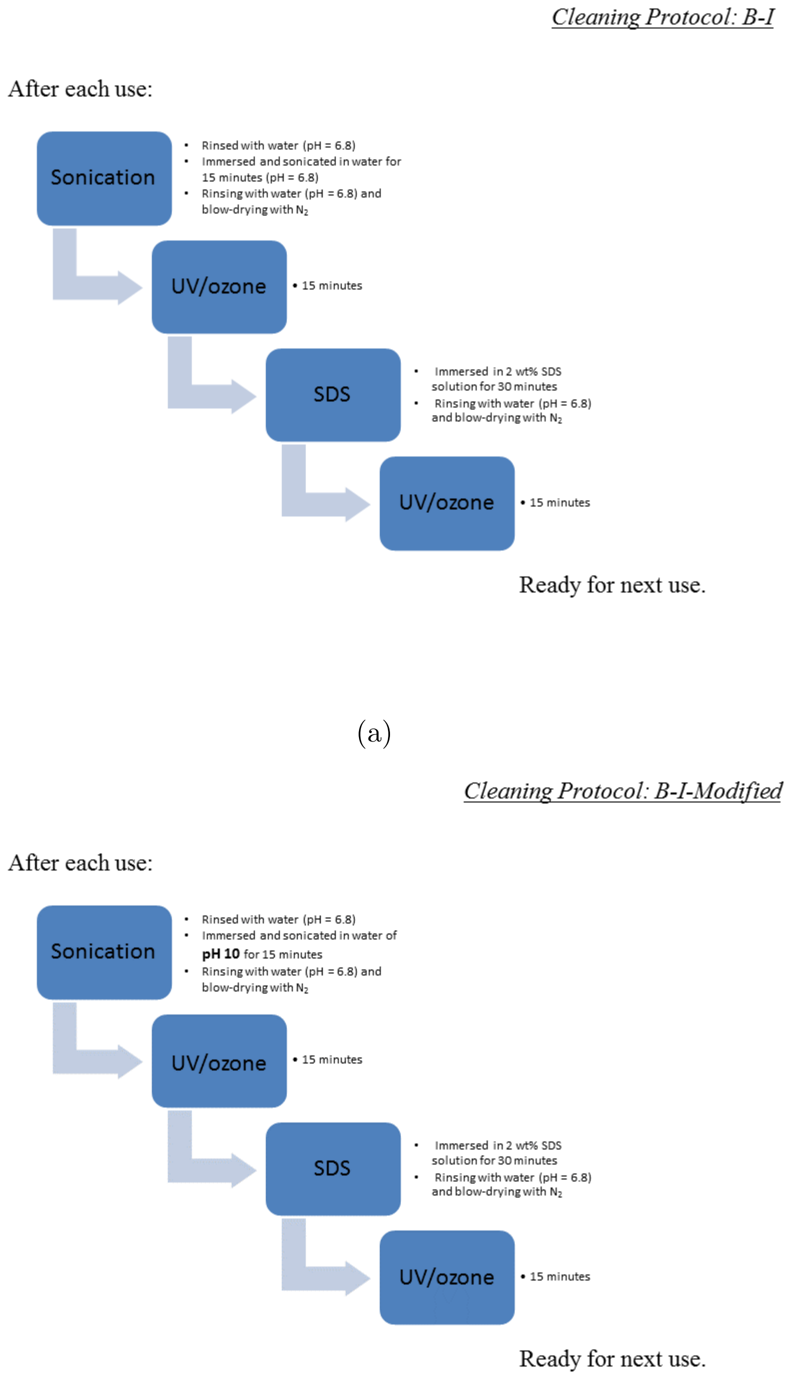

(a)

(b)

Figure 4.5: Conventional (a) vs Modified (b) cleaning protocol.

the time evolution of frequency even after one use of the sensors (see Figures 4.6 and 4.7):

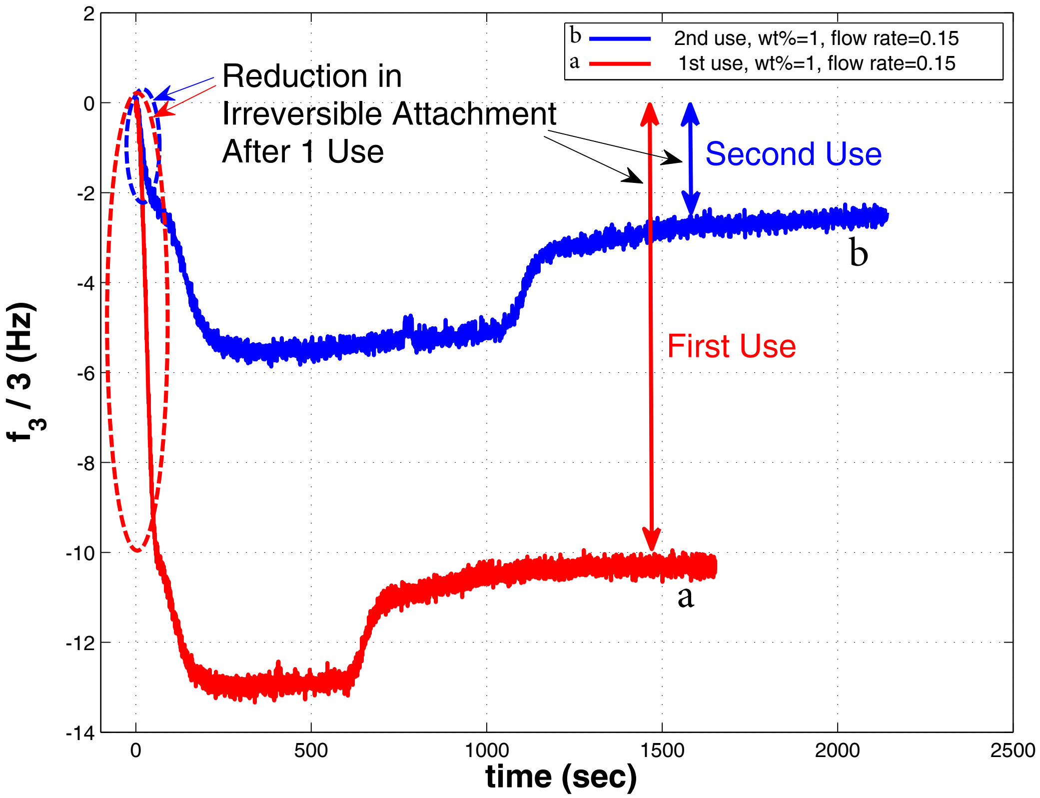

Figure 4.6: Reduction in the equilibrium amount of deposited particles following the conventional cleaning protocol: The blue graph (marked as 'b') shows that even for the 2nd use (i.e., after just 1 use) of a new sensor, almost all the particles reversibly attach onto the sensor surface as they were washed off during the rinsing step.

1. Considerable change of the net total frequency shift, both before and after the rinsing step.

2. Considerable change of the response of the sensor to the deposition of NPs (i.e., change of the behavior of frequency-time graphs). More precisely, by repeating an identical experiment on a single sensor, the aforementioned steep stage in the clean sensor bimodal graph gradually disappears and the frequency shift turns to a reversible-unimodal distribution in which

the attached particles were washed off during the rinsing step which is an indication of reversible attachment.

These observations confirm that the sensor surface undergoes gradual changes as the experiment is repeated over and over. We propose that the first monolayer which was attracted and bonded to the sensor surface is not properly removed using the conventional cleaning procedure which leads to "blocking" of the sensor surface. To systematically investigate this speculation, we first refer to the zeta potential of silica (the collector) and ceria (the particles) as a

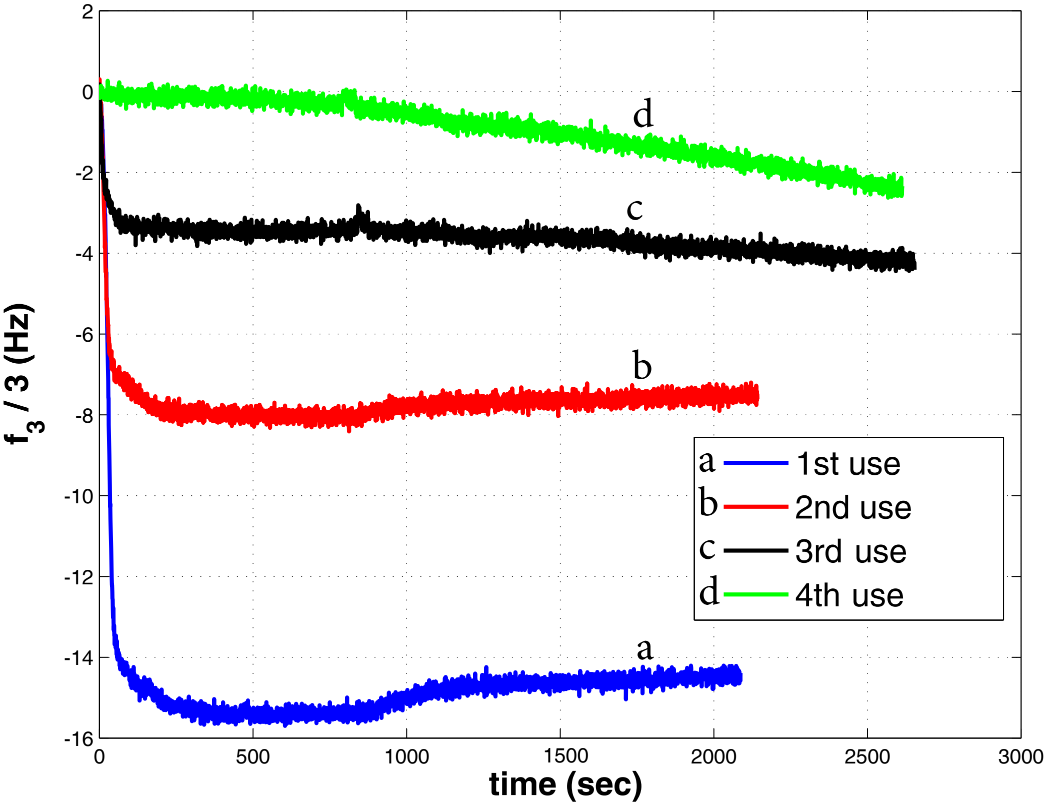

Figure 4.7: Reduction in the equilibrium amount of deposited particles following sequential use of the conventional cleaning protocol: The graphs show progressive coating of the sensor which results in reduction in the irreversible attachment. Specifically, after 1 use, the frequency shift changes to 50% of the corresponding value of a new sensor, and after 4 or 5 use no deposition is observed. This may happen even sooner, depending on the history of the usage of the sensor.

function of pH as reported in reference [1], as shown in Figure 4.1. According to this graph:

- Ceria attaches to silica at pH 3, where they have opposite charges: apparent in the experiments performed using new, clean silica coated sensors.
- Performing any step of the conventional cleaning (e.g. rinsing the sensor with DI water, sonicating it in DI water or SDS solution, etc.) at pH 7 does not remove the particles from the sensor surface, as they still bear opposite charges and hence are irreversibly attached to each other.

As a result, we modified the cleaning process by adding a simple step of sonicating the used sensors in a pH 10 solution as shown in Figure 4.5b. Evidently, adding this simple step causes the particles (which now bear the same charge as the sensor) to be completely removed from the sensor surface, leading the used sensor behave as a new one. As confirmed by Figure 4.8, the proposed cleaning causes the used sensors to act as new ones for at least 3 usages. After that, the sensors' behavior starts to deviate from new ones (probably due to dissolution and/or change of silica coating (as solubility of silica rapidly increases at pHs higher than 9 [58])).

It is worth noting that for the system studied here, the sensors should undergo the modified cleaning while kept wet, immediately after use (i.e., without having the chance to dry). An attempt to clean an old, already coated sensor by the modified cleaning protocol was unsuccessful.

In summary, zeta potential measurement (of the material of the sensor coating and the materials in the solution) should be done before performing adsorption/deposition experiments with QCM-D so that a cleaning procedure can be chosen to ensure that the sensors are cleaned properly. Otherwise, the deposited particles remain on the sensor surface, change the sensor surface properties and cause discrepancies in the results.

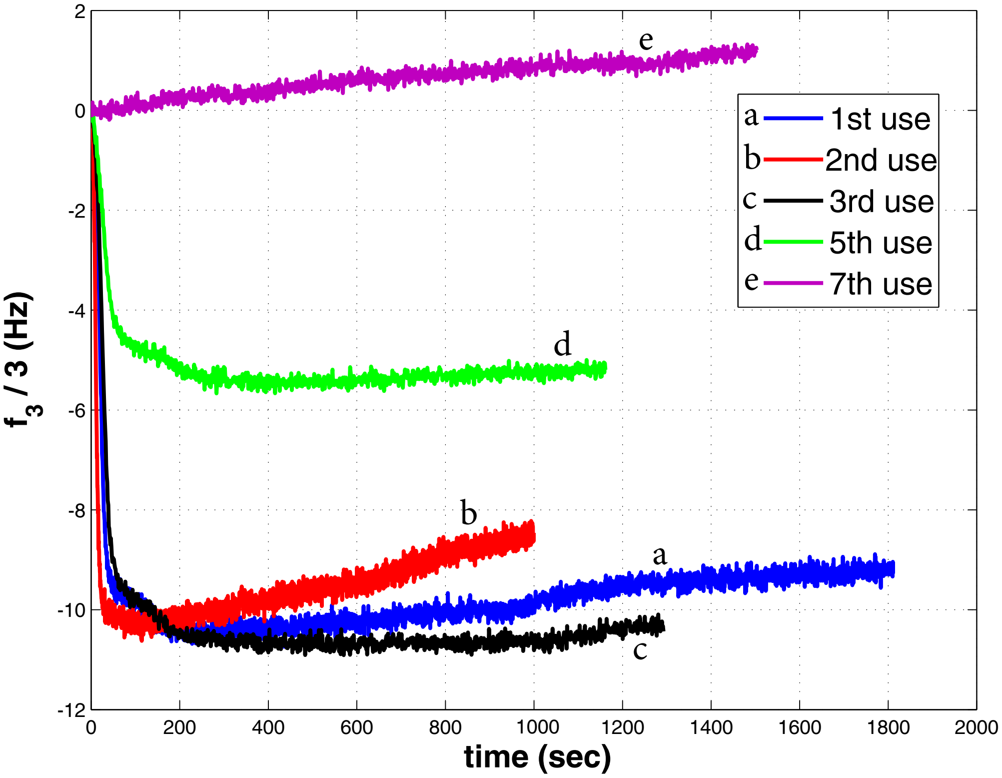

Figure 4.8: Repeatability of the equilibrium amount of deposited particles following sequential use of the modified cleaning protocol.

4.3 Ceria Deposition Dynamics on Clean Silica

4.3.1 Frequency and Dissipation Change in QCM-D Measurements

A typical graph obtained from one of the QCM-D measurements is shown in Figure 4.9 where five phases are identified. During phase I, Milli-Q water with the adjusted pH and the desired flow rate for the experiment is pumped into the sensor chamber to establish the baseline. The system is considered to be stabilized when the normalized 3$^{\text{rd}}$ overtone frequency shift ($\frac{\Delta f_3}{3}$) is less than 1 Hz for at least 5 minutes. During phase II, the sample (ceria suspension with the desired concentration and pH) is pumped through the system at the

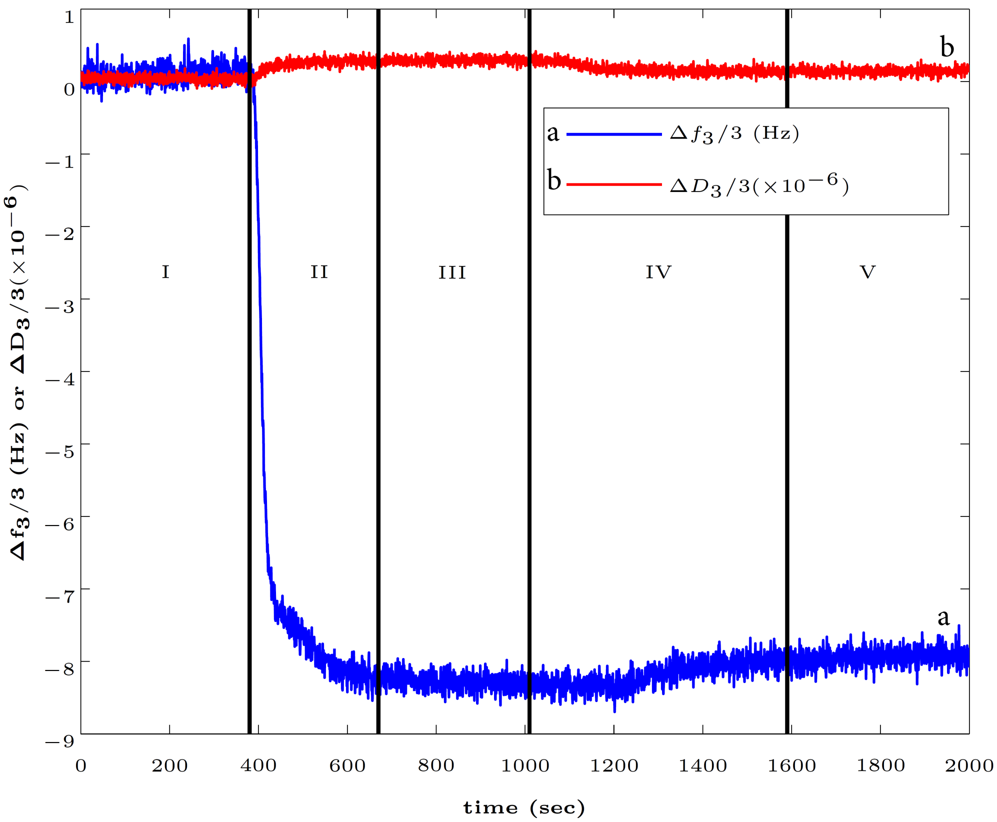

Figure 4.9: A typical graph showing the recorded changes in f_3 and D_3 during a QCM-D measurement at pH 3, ceria concentration of 0.1 wt%, and flow rate of 0.15 mL/min.

same flow rate. The system is allowed to equilibrate for at least 5 minutes after observing the interaction between the particles and the sensor (phase III). Then, the sensor surface is rinsed with Milli-Q water with the same pH and flow rate so that the reversibly attached particles detach from the sensor surface (phase IV). Rinsing is continued until equilibrium is reached in phase V. AFM and SEM images of the sensors are taken after phase V. As ceria particles are deposited onto (or released from) the sensor surface, the mass change of the crystal induces a proportional change in the n$^{\text{th}}$ overtone frequency (f_n) and amount of energy loss (which is reflected in dissipation (D_n)).

Since the rate of change of frequency during the initial deposition stage (i.e., stage II) is an indication of the rate of mass change during this stage, the initial slope of the corresponding graphs in stage II was used for kinetic study of the deposition process. As a general rule, the addition of a perfectly rigid mass to the crystal surface will yield zero additional D. As films of adsorbed nanoparticles are not necessarily rigid [59], a change in dissipation (D) may also be observed and used for studying the deposition process. Deposition rates, the slopes of the normalized frequency shift (Slope$_f$) and the normalized dissipation shift (Slope$_D$) were calculated from the data obtained during the initial portion of phase II. Both Slope$_f$ and Slope$_D$ were used simultaneously to compare deposition rates under different conditions. To interpret the results, it should be noted that larger absolute values of Slope$_D$ and Slope$_f$ are indicative of higher ceria deposition rates. As Slope$_f$ and Slope$_D$ were generally in agreement, Slope$_f$ is mainly presented and discussed here. Meanwhile, to make the results easier to follow, Slope$_f$ (in Hz/s) is converted to the rate of mass uptake per unit area of the sensor (in ng/cm^2.s) using the Sauerbrey equation, even though it is known not to be the best approach when studying deposition of nanoparticles.

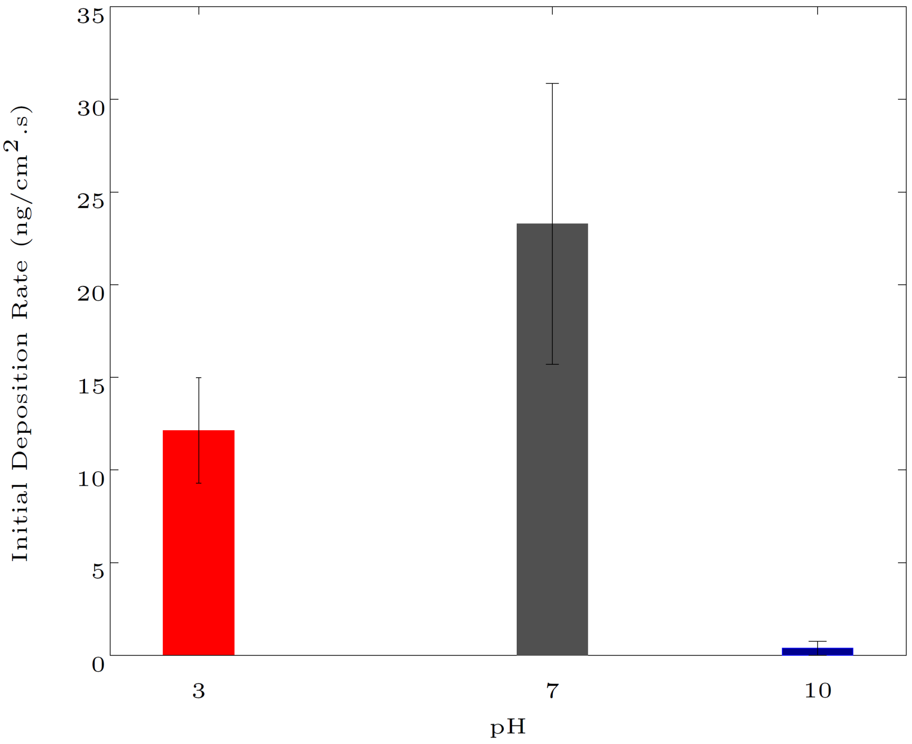

Figure 4.10: Effect of pH on the initial deposition rate based on the Sauerbrey conversion of Slope$_f$.

4.3.2 Effect of pH

Figures 4.10 to 4.12 show the effect of pH on the deposition of ceria on silica. The silica sensor has a negative charge for all pH values, while at pH 3 and 7, ceria particles are positively charged. At pH 10, both the particles and the sensor bear a negative charge [1]. Hence, pH 3 and 7 are representatives of favorable (attractive) conditions for the attachment of ceria to silica and pH 10 is representative of a repulsive condition as is shown by the initial attachment rates shown in Figure 4.10 (error bars represent the standard error).

Figure 4.10 shows the initial slope of the normalized sensor frequency change over time which is converted, using the Sauerbrey equation, to the rate of mass change during the initial stage of the deposition process. According to Figure

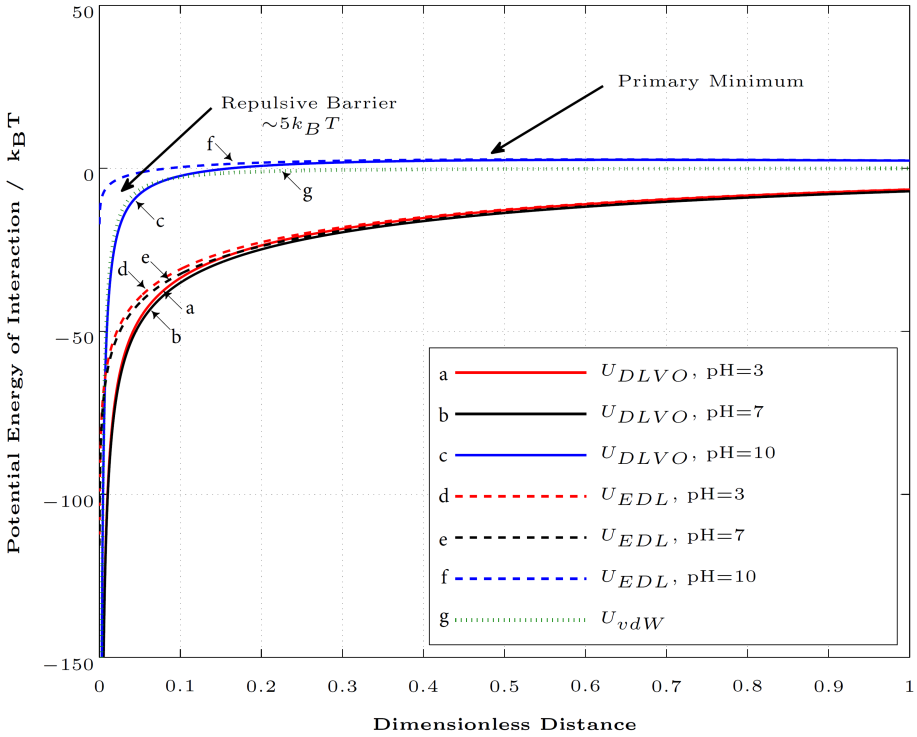

Figure 4.11: Effect of pH on DLVO interaction energy for a ceria nanoparticle approaching the flat silica surface. Abscissa is the dimensionless separation distance (i.e., the distance of closest approach between the particle and the sensor surface normalized by the diameter of the particle) between the spherical particle and the sensor.

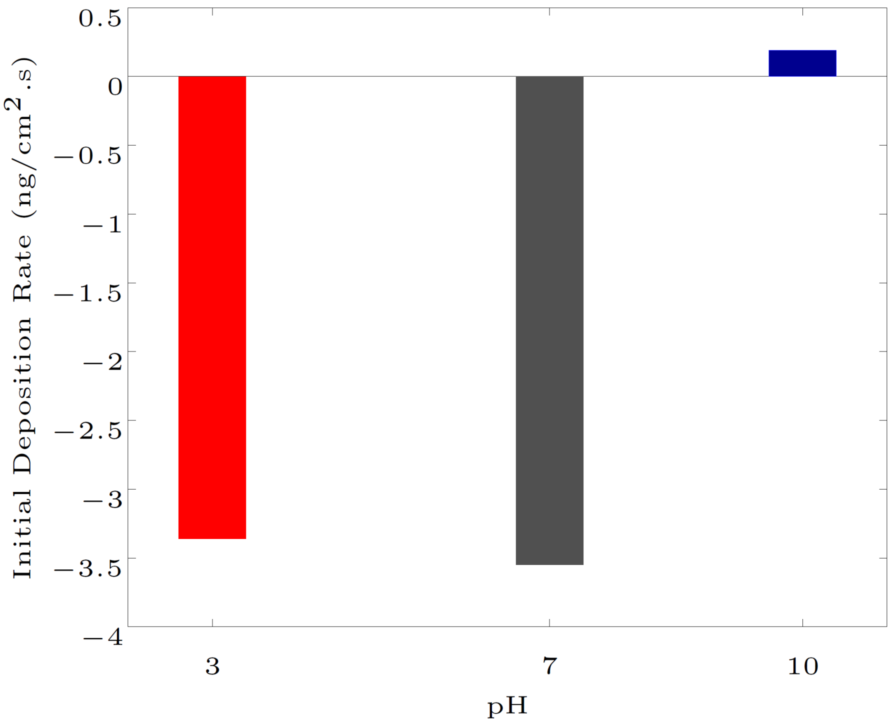

Figure 4.12: Simulation results for the initial deposition rate under different pH conditions (negative values indicate the movement of particles toward the sensor and vice versa).

4.10, much higher deposition rates are observed at pH 3 and 7 compared to pH 10 which is consistent with interaction energy analysis of the DLVO theory presented in Figure 4.11 as well as the results of numerical solution of the full governing transport equation presented in Figure 4.12. Figure 4.11 illustrates the dimensionless total interaction energy curves (i.e., the total interaction energy normalized by the thermal energy of the system) obtained from the summation of attractive vdW potential and electrostatic potential under the aforementioned three different pH conditions. The corresponding MATLAB codes are given in Appendix A. The vdW potential is identical for all three cases as it only depends on fixed system properties such as Hamaker constant and particle size. One characteristic of the vdW potential is that it decays with the distance between the particles and the sensor (See Equation 2.6). On the other hand, electrostatic potential varies with the pH of the solution which in turn affects the surface electric potential and surface charge of the particles. Electrostatic potential exhibits an exponential decay behavior which is influenced by the distance between the particles and the sensor as well as the inverse Debye length (κ) (See Equation 2.5). Therefore, the vdW attraction force dominates at very small and very large separation distances whereas electrostatic force (either repulsion or attraction) dominates at intermediate distances [60]. According to Figure 4.11, at pH 10, where both the particles and the sensor are negatively charged, the electrostatic potential forms a moderate repulsive barrier of $\sim 5k_BT$ which prevents the particles from approaching the sensor, leading to almost zero deposition. As the pH is decreased, the surface charge of the particles becomes positive and the electrostatic force changes from repulsion to attraction. Consequently, the particles can get close enough for vdW forces to act and promote the deposition of nanoparticles onto the sensor in the primary minimum. This is confirmed by the experimentally obtained deposition rates shown in Figure 4.10. However, not only does the final behavior of the system depend on the DLVO interaction energy analysis, but it also depends on the dynamics of the attachment process. In other words, when the deposition is energetically favorable (for example at pH 3), based on the interaction energy analysis, one can only predict that deposition might occur if the particles have the chance to collide with the sensor. Nevertheless, the particle-collector collision is the prerequisite for successful attachment and should be taken into account to explain the experimentally observed deposition rates. This is discussed in more detail in Section 4.3.3. As long as occurrence of enough particle-collector collisions is ensured by selecting appropriate experimental conditions, the initial deposition rates observed experimentally will agree with the results of DLVO interaction energy analysis. Figure 4.12 confirms that this is indeed the case for the system studied here. The initial deposition rate (calculated by integrating flux of particles at a distance equal to particle diameter from the sensor surface) is the highest at pH 7 (negative sign indicates that the flux of particles is toward the collector, i.e., in negative z-direction) where the attractive interaction energy is the strongest as shown in Figure 4.11. The initial deposition rate decreases at pH 3. At pH 10, the flux and consequently the rate appear to change from negative to positive, which is a demonstration of no deposition at pH 10.

These results are also confirmed by SEM images (Figures 4.13 and 4.14) taken from clean sensors after their exposure to particle suspensions at pH 3, 7 and 10 (i.e., after phase V). As seen in these images, the most deposition occurs at pH 7 since the electrostatic attraction between the particles and the sensor is the highest at this pH (see Figure 4.11). At pH 3, deposition is still observed, but the extent of deposition is less than the case of pH 7. This is attributed to the weaker electrostatic attraction at pH 3 as compared to pH 7. It is also evident in Figures 4.13a and 4.13b that the particles are deposited on the sensor surface uniformly without local clustering. In other words, the particles form an irregular array on the surface. Meanwhile, ceria particles appear to be larger at pH 7 as compared to the case of pH 3. This is consistent with the fact that the zeta potential of the particles at pH 7 is less than pH 3 [1], leading to weaker particle-particle repulsion at pH 7 and formation of particle doublets and/or triplets (but not considerably large aggregates). On the contrary, ceria particles form large aggregates at pH 10 (as the mutual repulsion is the least at this pH), but as suggested by Figure 4.13c, they cannot surmount the energy barrier formed by the electrostatic repulsion between the sensor and the particles. As a result, no particles were deposited on the sensor surface at pH 10. QCM-D frequency response as a function of time for different pH's (Figure 4.15) agrees with SEM images in Figures 4.13 and 4.14. To further confirm the results, AFM images of the sensors were also taken after their exposure to particle suspensions at the aforementioned pH conditions. Figure 4.16a shows the AFM image taken at pH 3. In an attempt to identify the position of the ceria particles deposited on the sensor, a Gaussian filter was first applied to the original image. This was then followed by applying a Gamma correction (power > 1) which made it possible to locate the particles. Figures 4.16b, 4.16c and 4.16d show the corresponding images for pH 3. Based on the location of the particles' centers, their radial distribution function ($g(r)$) was obtained to describe their local structure (Figure 4.16e). Figure 4.16e provides more evidence for the lack of local clustering and further confirms that the deposited ceria particles form an irregular array on the sensor surface at pH 3. Corresponding images and results for pH 7 and 10 are presented in Figures 4.17 and 4.18, respectively.

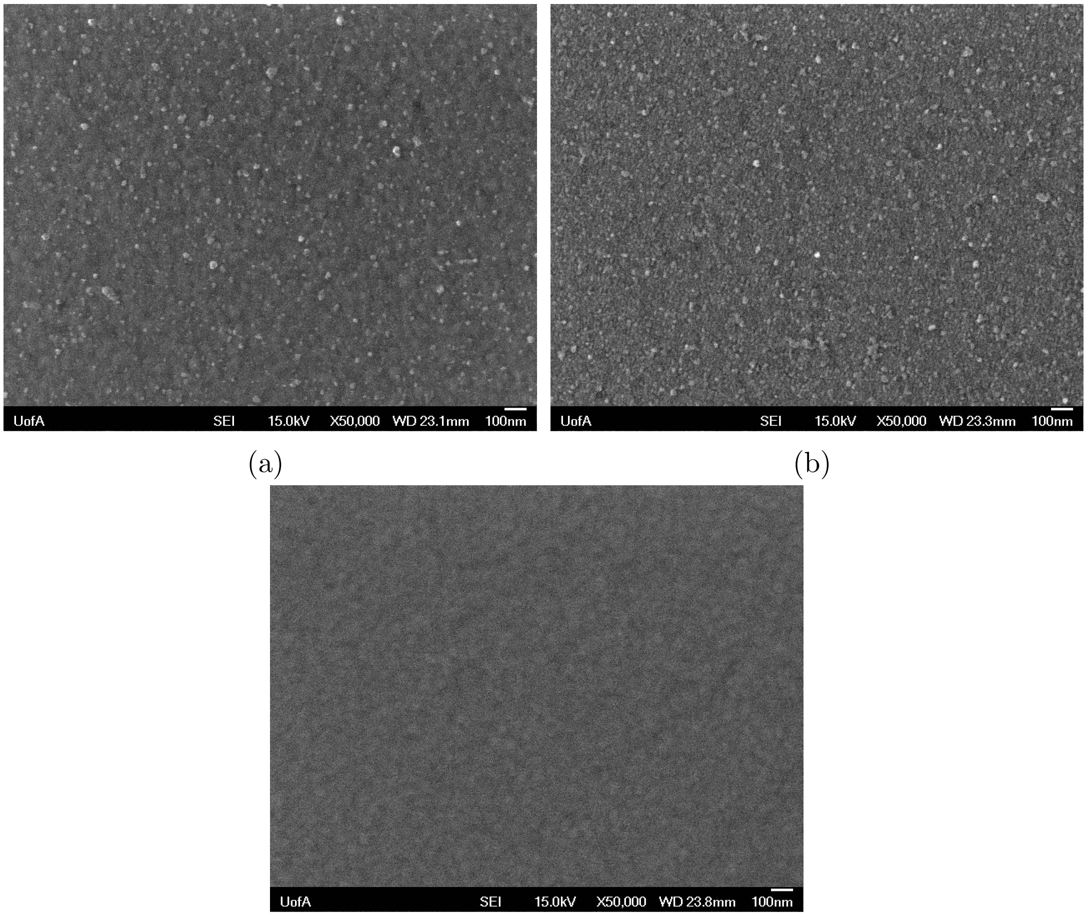

(a) (b)

(c)

Figure 4.13: (a) SEM image of deposited ceria particles on silica sensor at pH 3, (b) pH 7, (c) pH 10. The images are taken at 50000 magnification and correspond to deposition experiments done with 0.1 wt% suspensions.

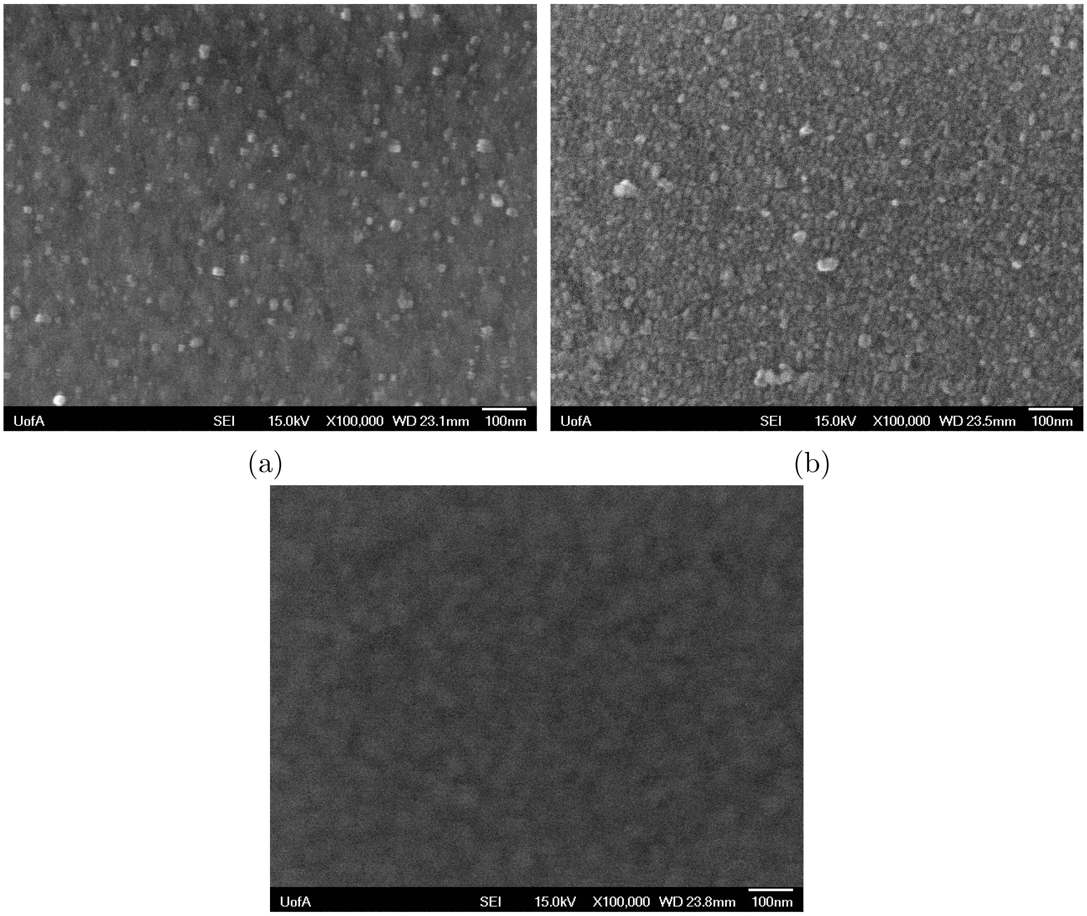

(a)

(b)

(c)

Figure 4.14: (a) SEM image of deposited ceria particles on silica sensor at pH 3, (b) pH 7, (c) pH 10. The images are taken at 100000 magnification and correspond to deposition experiments done with 0.1 wt% suspensions.

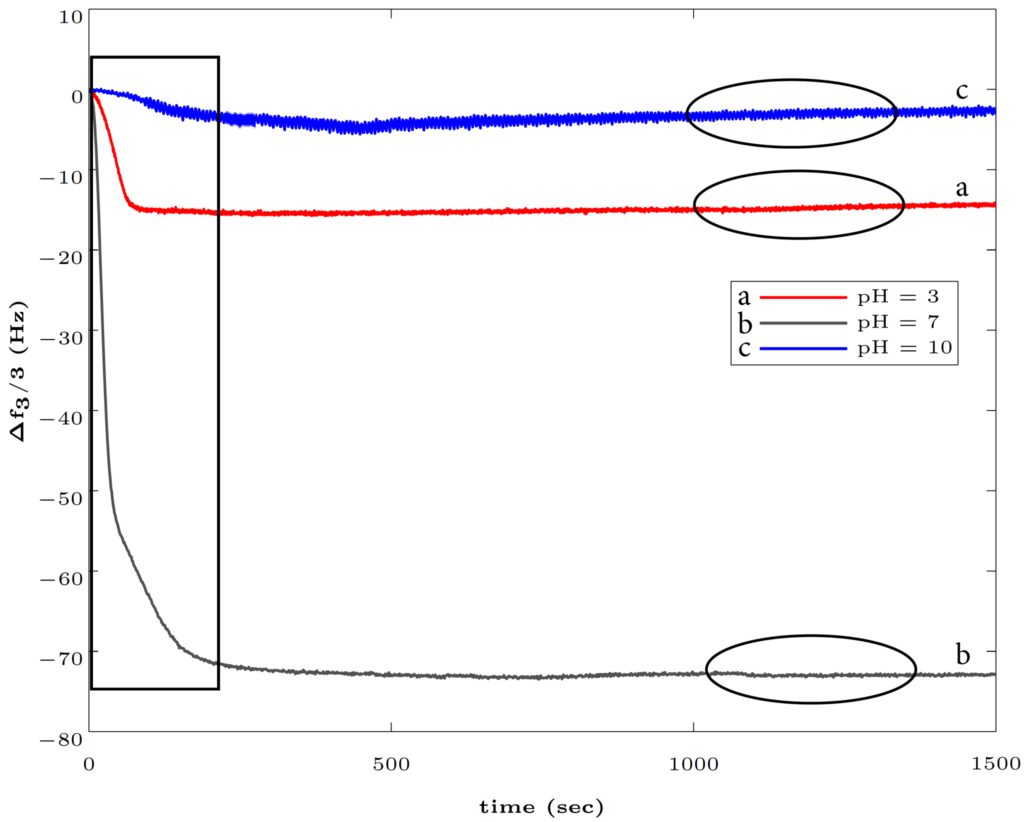

Figure 4.15: A typical graph showing the recorded changes in f_3 during three QCM-D measurements at pH 3, 7 and 10, ceria concentration of 0.1 wt%, and flow rate of 0.15 mL/min. The rectangle shows the part of the graph used for calculation of initial deposition rates, while the ellipses show the equilibrium amount of deposited particles on the sensor surface captured by SEM images.

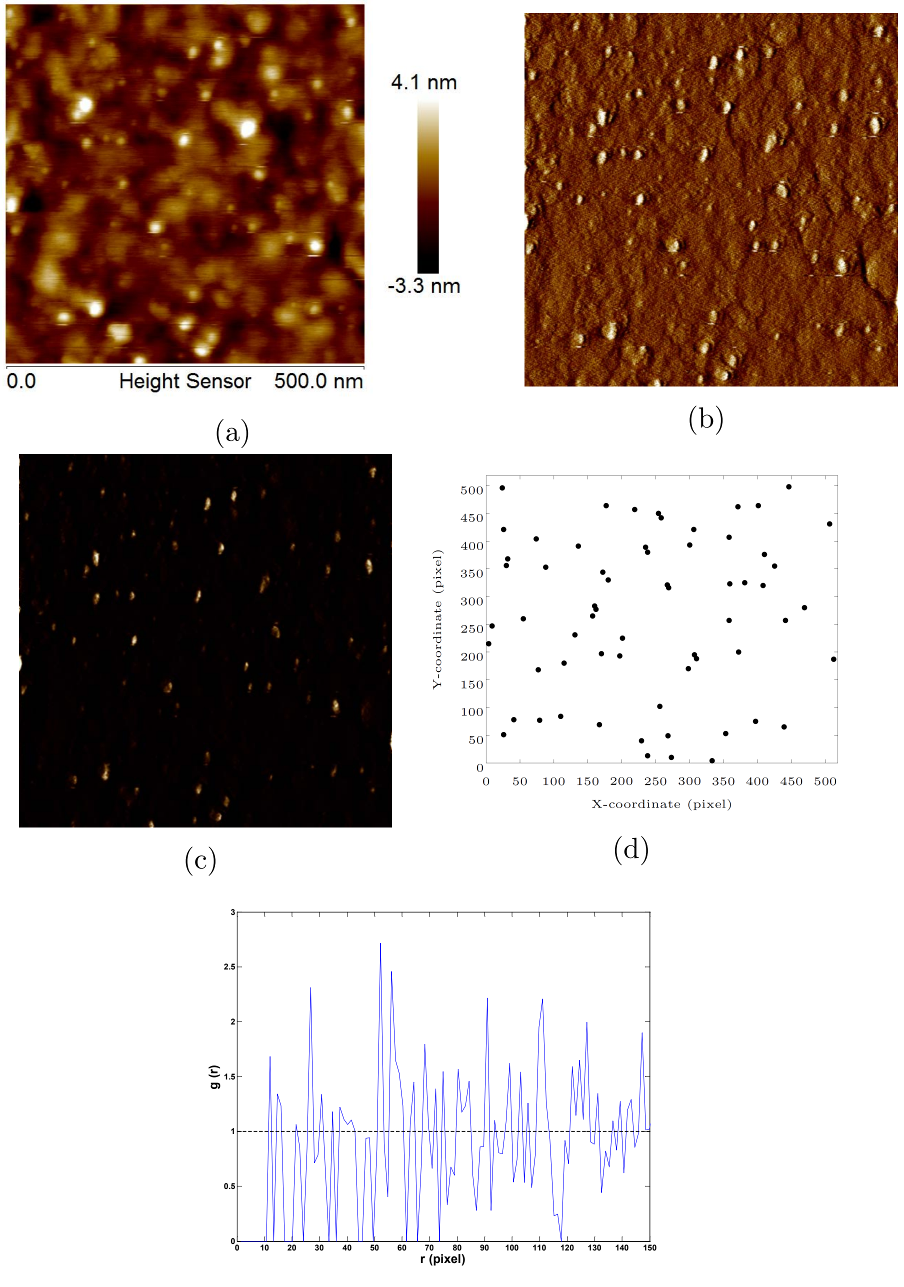

(a)

(b)

(c)

(d)

(e)

Figure 4.16: (a) AFM image of deposited ceria particles on silica sensor at pH 3, (b) Result of applying Gaussian filter on the original AFM image, (c) Result of applying Gamma correction on the previous image, (d) Position of deposited ceria particles on silica sensor at pH 3, (e) Pair distribution function of ceria particles at pH 3.

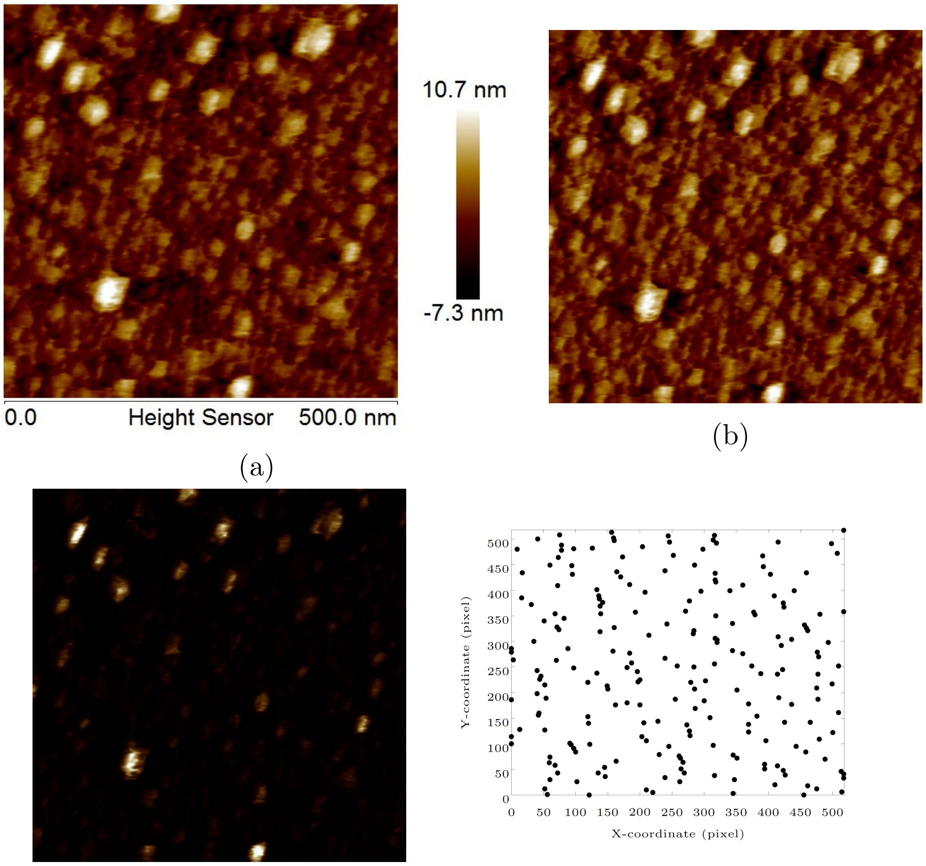

(a)

(b)

(c)

(d)

Figure 4.17: (a) AFM image of deposited ceria particles on silica sensor at pH 7, (b) Result of applying Gaussian filter on the original AFM image, (c) Result of applying Gamma correction on the previous image, (d) Position of deposited ceria particles on silica sensor at pH 7.

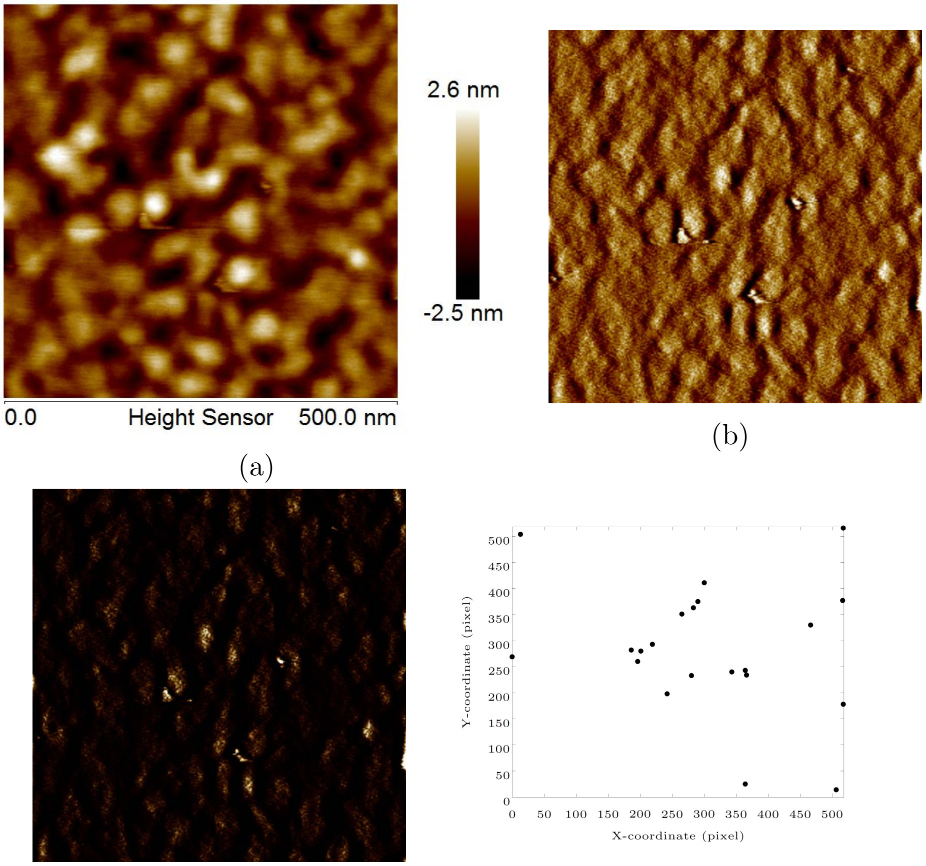

(a)

(b)

(c)

(d)

Figure 4.18: (a) AFM image of deposited ceria particles on silica sensor at pH 10, (b) Result of applying Gaussian filter on the original AFM image, (c) Result of applying Gamma correction on the previous image, (d) Position of deposited ceria particles on silica sensor at pH 10.

4.3.3 Effect of Flow Rate

To thoroughly investigate the deposition of ceria onto silica, an attempt was made to address the effect of the velocity field on the dynamics of the attachment process. Figures 4.19 to 4.21 show the effect of the velocity field on the initial rate of deposition of ceria on silica at pH 3. At this pH, DLVO forces are favorable for attachment and ceria suspensions exhibit excellent stability. Therefore, if there is an adequate opportunity for the particles to encounter the sensor or collide with the sensor, high deposition rates are anticipated.

Figure 4.19 confirms that at low ceria suspension flow rates, the rate of deposition is limited by the bulk flow which transports the particles to the sensor, even though the attachment is energetically favorable. Accordingly, as the flow rate is increased, deposition is more significantly controlled by the affinity of the particles to the sensor. Figure 4.20 also illustrates, quantitatively, the transition from transport controlled to affinity controlled deposition of ceria on silica by increasing the flow rate. It is clear from this figure that at flow rates greater than 0.15 mL/min the process is not limited by the transport of ceria particles to the QCM-D crystal. For this reason, a flow rate of 0.15 mL/min was chosen as the optimum experimental condition for investigating the effect of other parameters on the interaction of ceria and silica. Simulation results, presented in Figure 4.21, successfully predict the experimentally observed behavior. Namely, as the flow rate is increased, the absolute value of the initial deposition rate increases.

In spite of the short-term deposition behavior, the equilibrium frequency shift was observed not to be influenced by altering the flow rate (results are shown in Figure 4.22). Hence, the long-term behavior of the system is not affected by altering the flow rate.

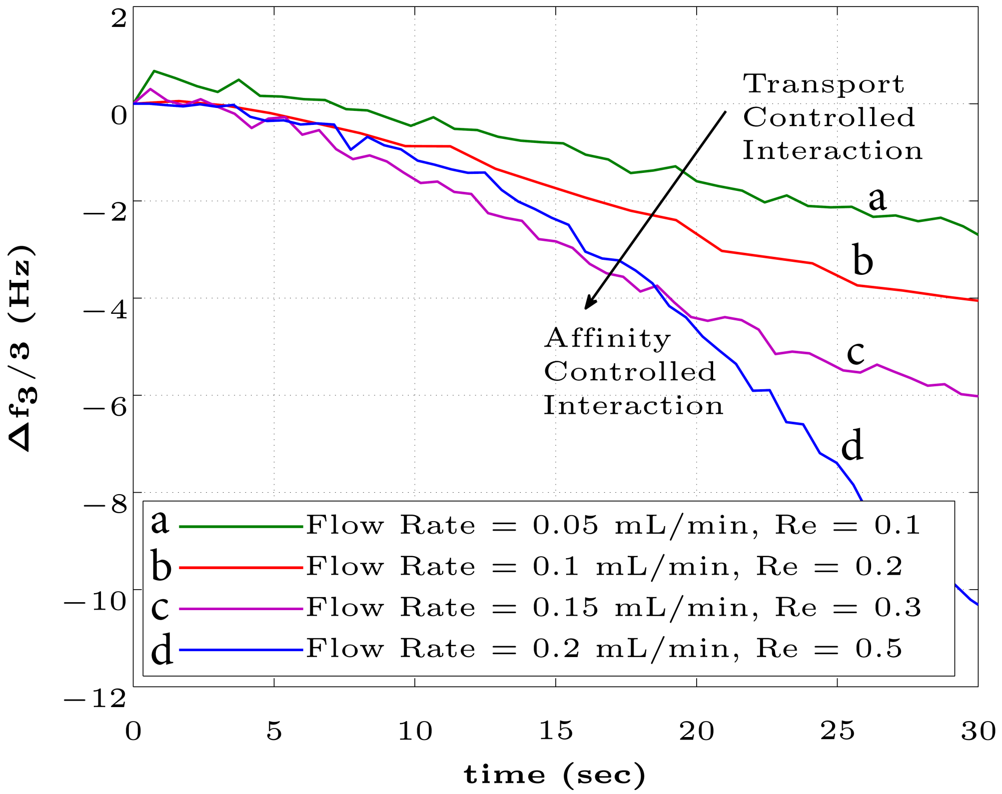

Figure 4.19: Qualitative representation of the effect of flow rate on the kinetic of the deposition process; pH is 3 and ceria concentration is 0.1 wt%.

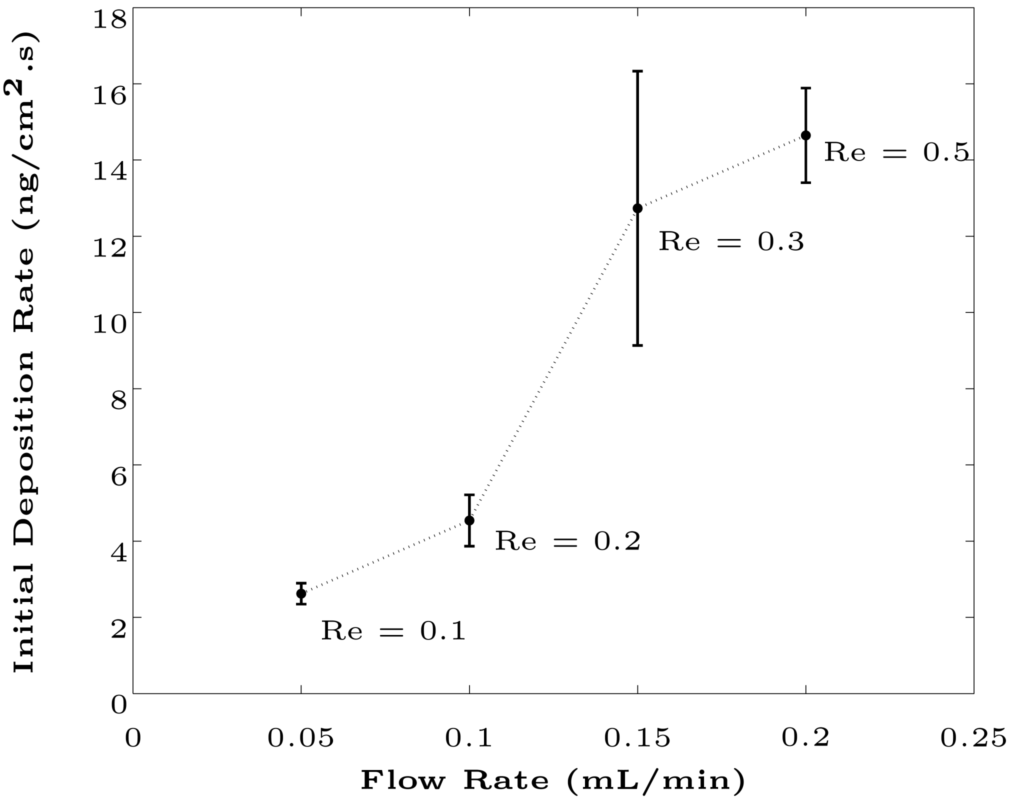

Figure 4.20: Effect of flow rate on the kinetic of the deposition process based on Sauerbrey conversion of Slope$_f$; pH is 3 and ceria concentration is 0.1 wt%.

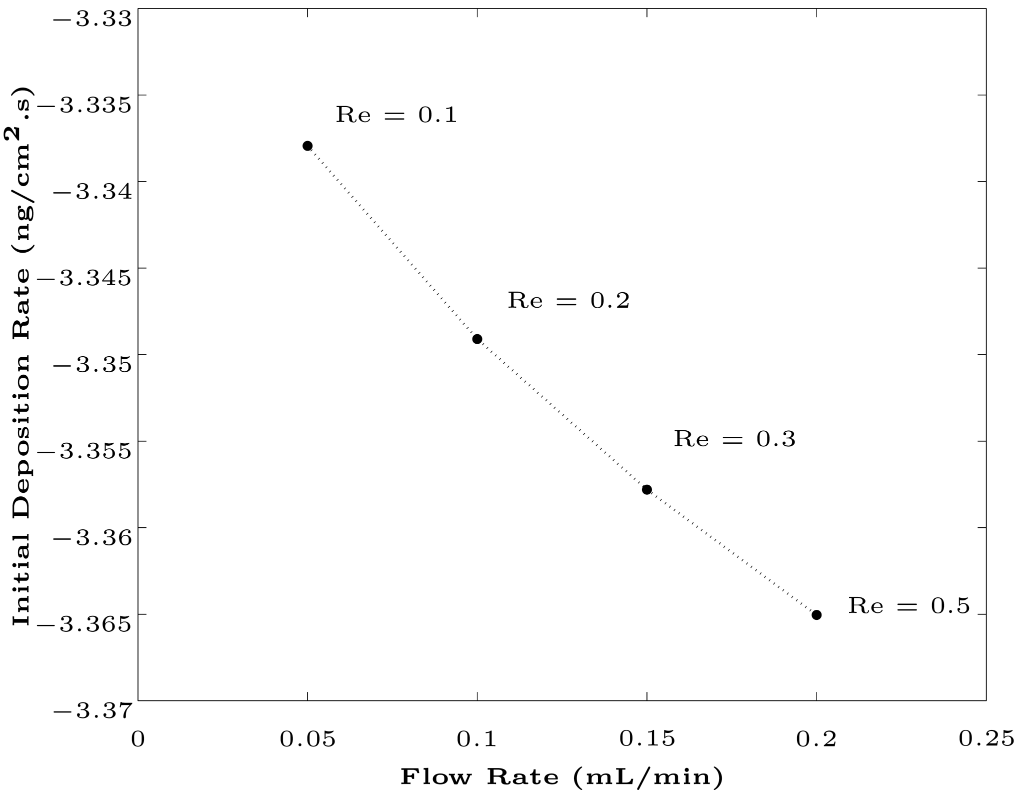

Figure 4.21: Simulation results for the initial deposition rate as a function of background fluid flow velocity (negative values indicate the movement of particles toward the sensor and vice versa).

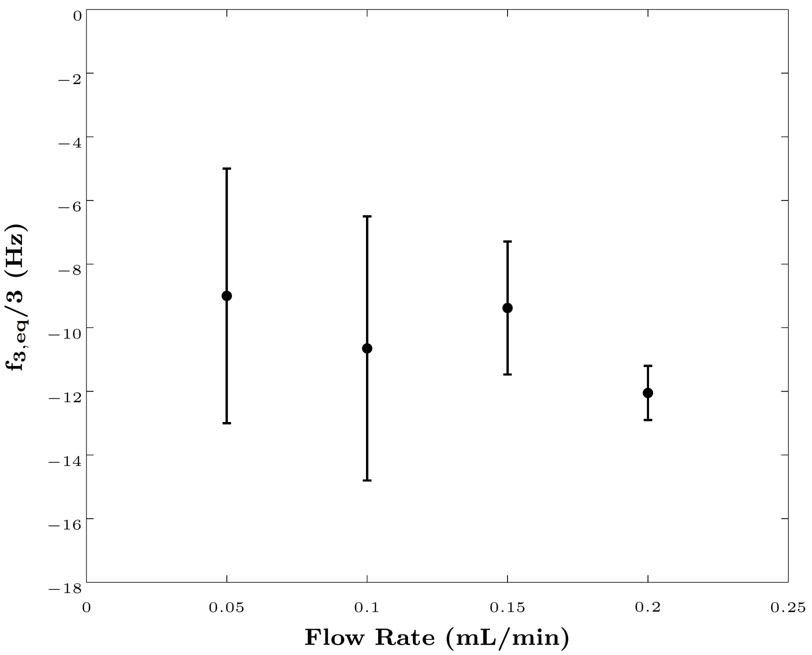

Figure 4.22: Effect of flow rate on the equilibrium frequency shift obtained from QCM-D measurements; pH is 3 and ceria concentration is 0.1 wt%.

4.3.4 Effect of Ceria Concentration

Figures 4.23 and 4.24 show the effect of ceria bulk concentration on the initial deposition rate at the optimum flow rate of 0.15 mL/min and pH 3, where attachment of ceria to silica is favorable and the particle suspensions exhibit excellent stability. Figure 4.24 demonstrates that, to the extent that the governing transport equation holds, increasing bulk concentration of ceria particles results in an increase in the theoretical initial deposition rate. However, Figure 4.23 shows that the initial deposition rates obtained experimentally from QCM-D measurements exhibit complex behavior. The results are also shown together in Figure 4.25. To make the comparison easier in Figure 4.25, simulation results represent the *absolute* value of the initial deposition rate taken from Figure 4.24.

Increasing ceria concentration increases the collision frequency of the particles with the sensor, which results in higher deposition rates. This is consistent with the numerical simulation results as well as the behavior of the experimental system within the intermediate region of bulk concentrations studied here.

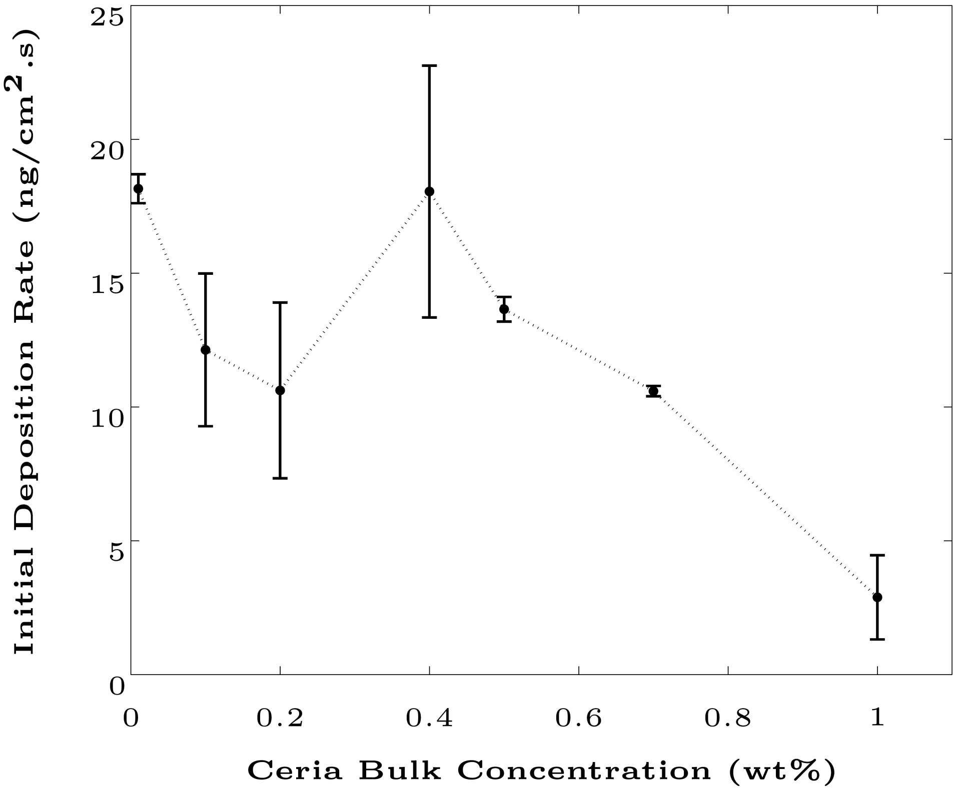

Figure 4.23: Effect of ceria concentration on the kinetic of the deposition process based on Sauerbrey conversion of Slope$_f$; pH is 3 and flow rate is 0.15 mL/min.

For the regions of low and high ceria bulk concentration studied in this work, the initial deposition rate decreases with increasing the bulk concentration of ceria NPs. Explaining these results necessitates the use of more sophisticated models for the transport of NPs from flowing suspensions toward the collector. To this end, mutually repulsive particle-particle interactions should be incorporated into the full governing transport model to enable it to predict the experimentally observed behavior of the system. In more concentrated ce-

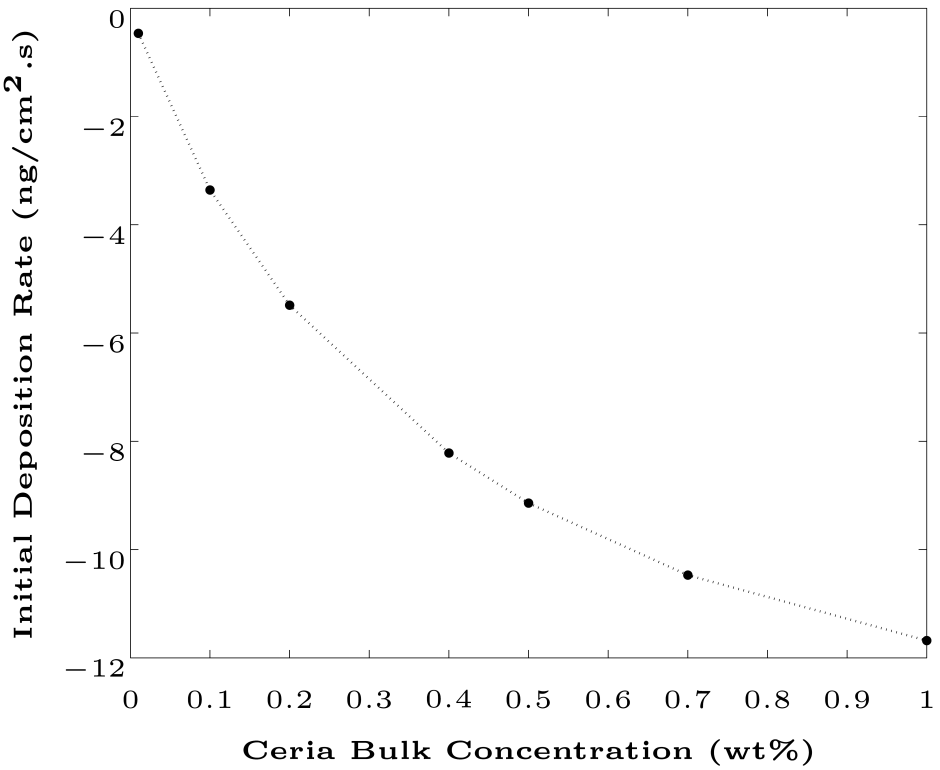

Figure 4.24: Simulation results for the initial deposition rate as a function ceria bulk concentration (negative values indicate the movement of particles toward the sensor and vice versa).

ria slurries, particle-particle interactions will be more pronounced (due to the greater population of particles) which lead to the ceria particles being more scattered and reducing their ability to collide with the sensor compared to the case of infinitely dilute suspensions. Hence, the experimentally obtained variations in deposition rate by varying ceria concentration can be attributed to many-body interactions between ceria particles, which are ignored in DLVO theory and subsequently in the convection-diffusion-migration model.

Similar behavior has been reported in literature [61] but the correlation of this behavior with colloidal interaction energies and particle-particle collisions was not fully explored.

The observed behavior can also be attributed to the specific attachment of

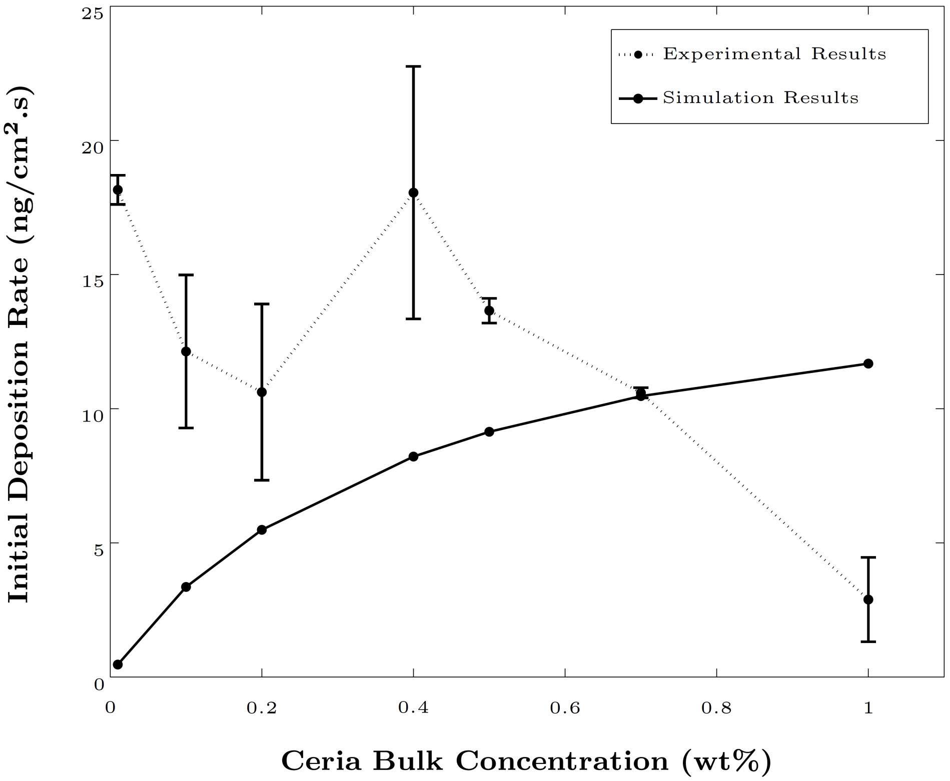

Figure 4.25: Effect of ceria concentration on the kinetic of the deposition process based on both Sauerbrey conversion of Slope$_f$ and simulations at pH 3 and flow rate of 0.15 mL/min. To make the comparison easier in this figure, simulation results represent the *absolute* value of the initial deposition rate taken from Figure 4.24.

species. However, based on the current knowledge, although various attempts has been made to study such effect, only chemical bonding, hydrophobic interactions, and some solvation effects in specific systems have been quantified [51]. For the system at hand, these interactions may include specific attachment of the counter-ions, present in the ceria suspension, to silica as well as chemisorption of ceria to silica.

The trade-off between the aforementioned counteracting effects determines the experimentally observed initial deposition behavior of the system.

Similar to the case of varying the flow rate, investigation of the long-term

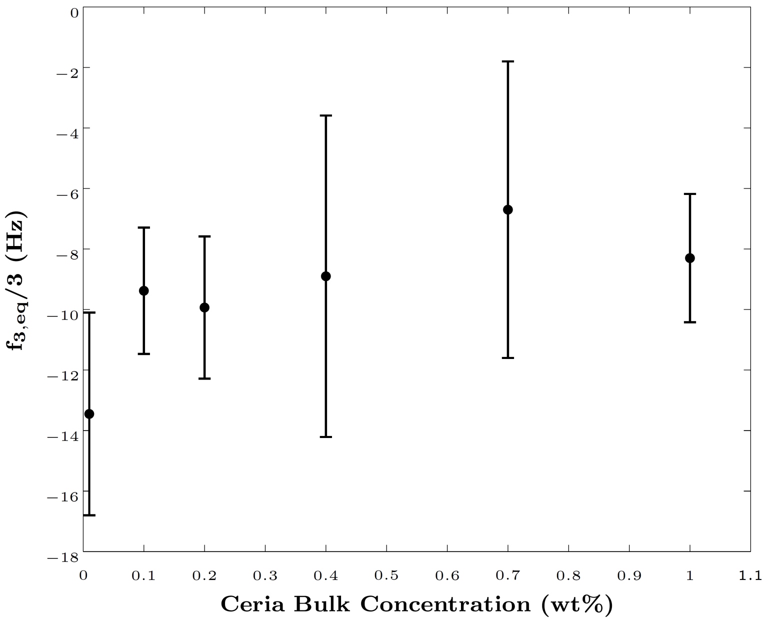

Figure 4.26: Effect of ceria concentration on the equilibrium frequency shift obtained from QCM-D measurements; pH is 3 and flow rate is 0.15 mL/min.

deposition behavior of the system reveals that the equilibrium amount of ceria attached to silica is not affected by the concentration of ceria nanoparticles in the bulk (results are presented in Figure 4.26). In other words, regardless of the bulk concentration of ceria nanoparticles, the same amount of surface coverage is eventually achieved by continuous supply of particles and by letting the system to reach steady state. Similar results have been reported in other studies [61], while the opposite has also been reported in literature [62].

Chapter 5

Conclusions and Future Work

5.1 Conclusions

The present study is aimed at the development of a comprehensive approach for investigating the effect of hydrodynamic factors (such as fluid flow velocity) and non-hydrodynamic factors (such as the interactions between the particles themselves and the interactions between the particles and surfaces) on the interactions of abrasive particles in CMP slurries. To perform a systematic analysis of the mutual influence of these factors and assess the pertinent transport behavior, we resort to both experimental studies in a well-defined system and computer simulations. Two commonly encountered materials in CMP slurries, silica and ceria, are chosen for this purpose. The key findings of this work are summarized as follows:

- When dealing with charged moieties, zeta potential measurements (of the material of the sensor coating and NPs in the suspension) should be done prior to performing adsorption/deposition experiments with QCM-D so that a cleaning procedure can be chosen to ensure that the sensors are reused properly. Otherwise, the deposited particles remain on the sensor surface, change its surface properties and cause discrepancies in the results.

- Effect of pH: Both short-term and long-term behaviors of the system are strongly affected by pH. Altering the pH changes surface charge properties of the interacting moieties. As a result, electrostatic double layer interactions are affected. Pursuing this further, the system exhibits considerably different behavior when these interactions change from attraction to repulsion.

- Effect of flow rate: Deposition dynamics is affected by the flow rate. However, for the range of flow rates studied here, variation of the flow field does not affect the equilibrium amount of deposited ceria particles onto silica surface.

- Effect of ceria bulk concentration: In this case, the initial short-term behavior is different from the long-term deposition behavior. The results indicate that considering many-body interactions between the particles is necessary for accurate prediction of the behavior of the systems in which interplay of both repulsive and attractive electrostatic interactions exists.

5.2 Future Work

Based on the results obtained in this work, it is evident that the effect of ceria concentration on the attachment of ceria to silica requires further study.

The QCM-D experiments performed in this work involved a rising step at the same pH at which the attachment had happened. To investigate the effect of pH on the release of attaced NPs from the sensor surface, this rinsing step may be followed by another rinsing step at a desired pH. Such studies shed light on the effect of pH on the cleaning after CMP.

Another possible direction for future research is the study of the short-term and long-term stability behavior of ceria-silica MAS using other techniques and/or model systems (such as light transmittance measurements combined with well-controlled settling tests).

Moreover, simultaneous use of QCM-D and spectroscopic ellipsometry, which can detect submonolayer changes in thickness of nanometer scale films, is a promising multitechnique approach for studying and characterizing nanoparticle interactions and is likely to provide complementary information on the attachment of ceria to silica.

The lack of an appropriate approach for converting QCM-D raw data (specifically, temporal changes of frequency) to the mass uptake by the sensor beyond Sauerbrey equation is a major issue. Development of comprehensive models to address this issue requires further experimental and theoretical study. Accordingly, the following section attempts to provide a general framework to accomplish this task by proposing an "extended governing transport equation" and suggesting an outline for converting frequency shift to mass when studying nanoparticles attachment using QCM-D.

5.2.1 Converting Frequency Shift to Mass Beyond Sauerbrey Equation

As was mentioned earlier, the governing transport model and the numerical results discussed in this work were based on a major assumption that the sensor surface is absolutely clean and the particles *do not* accumulate on the sensor surface upon their deposition. Therefore, this model applies *only* to the initial stage of the deposition process on a clean sensor. Hence, numerical solution of this model gives an *upper bound* for the flux of colloidal particles toward the sensor. Nonetheless, as long as one performs the experiments on a clean sensor and calculates initial rate of deposition from the raw experimental data, the experimental data can be used to validate the model and the model, thereafter, can be used to predict the short term deposition behavior of the system. Otherwise, the model must be modified to account for the sensor surface becoming less favorable for attachment as deposition proceeds. General explanations for applying such a modification is discussed here. By applying such a modification, not only does the ability of the model in interpreting experimental deposition data increase, but also a unique way for fitting raw frequency-time data and obtaining fractional surface coverage and deposited mass when using QCM in NP research will be achieved. It was also pointed out in Section 4.2 that lack of proper cleaning of the sensors between the QCM-D measurements will completely change the properties of the interacting materials and hence, will lead to erroneous conclusions about the forces of interaction present in the system. It is worth noting that this procedure is not supposed to, but still may potentially be useful to, correct for such experimental faults.

Extended Governing Transport Equation

Transport of nanoparticles over collector surfaces is explained by a 2-D convection-diffusion model taking into account the effect of temporal changes in collector surface which affect DLVO interaction of NPs and the collector surface as the surface is covered by NPs.

The general governing equation for this process is:

$$\frac{\partial n}{\partial t} = \nabla.(-\vec{V}n + \bar{\bar{D}}.\nabla n) - R_a \tag{5.1}$$

where n is the number concentration of NPs in the suspension, $\vec{V}$ is the particle velocity, $\bar{\bar{D}}$ is the diffusion coefficient tensor, and R_a is the term that accounts for attachment and release of NPs onto the collector surface as the deposition proceeds.

We demonstrate the deposition and release of NPs by:

$$S \underset{k_d}{\overset{k_a}{\rightleftharpoons}} A \tag{5.2}$$

where k_a and k_d denote the attachment and release rate constants, S corresponds to the NPs in the solution and A corresponds to the attached NPs. Furthermore, R_a, which is the time evolution of surface concentration of deposited NPs, can be expressed as:

$$R_a = F[k_a B(\theta)n - k_d C_A] = F[\frac{dC_A}{dt}] \tag{5.3}$$

where $B(\theta)$ is an indication of the available surface area for deposition of NPs as the deposition proceeds and C_A denotes surface concentration of deposited NPs. F is assumed to be unity for now, but in general a value can be assigned to it depending on the system in which deposition process is taking place. Assuming the particles to be spheres with radius a_p, C_A can be converted to the fractional surface coverage (θ) and the last equation can be re-written as:

$$\begin{aligned} \frac{d\theta}{dt} &= \pi a_p^2 k_a B(\theta)n - k_d\theta \\ R_a &= \frac{F}{\pi a_p^2}[\pi a_p^2 k_a B(\theta)n - k_d\theta] \end{aligned} \tag{5.4}$$

To account for the blocking behavior, Langmuir adsorption model can be employed, which results in:

$$B(\theta) = 1 - a_1\theta \tag{5.5}$$

It is accepted to be reasonable to assume $a_1 = 1$ for completely favorable attachment conditions, but in general a value can also be assigned to it depending on further investigations of the system. For such conditions, k_d may also be neglected.

Equations 5.1 and 5.4 can be simultaneously solved to obtain the theoretical time evolution of $n(x, z)$ and $\theta(t)$.

QCM-D experiments generate time evolution of f (frequency) as an indication of the mass of deposited particles over time. Although it has been previously proposed (for some specific systems, through experiments and FEM simulations) that the rate of surface coverage decreases as particles deposit on the collector surface, there is not yet an explicit formula or guideline to relate $f(t)$ to $\theta(t)$ for studying NPs attachment using QCM-D. Here. We try to establish such a relationship by fitting experimental $f(t)$ data and theoretical $\theta(t)$ (denoted by $\theta(t)_{th}$ from now on).

To this end, we propose a nonlinear relationship between experimental $f(t)$ and $\theta(t)_{exp}$ as:

$$\theta(t)_{exp} = 1 + b_1 f + b_2 f^2 + b_3 f^3 + \dots \tag{5.6}$$

We then try to fit $\theta(t)_{th}$ and $\theta(t)_{exp}$ by adjusting 4 parameters: b_1, b_2, b_3 and k_a. These steps are summarized in Figure 5.1. Hence, with the help of both experimental observations and computer simulations, we will be able to relate the effect of any desired experimental condition on the coefficients of Equation 5.6 which may shed light on the synergistic or antagonistic effect of simultaneous variations in several experimental variables.

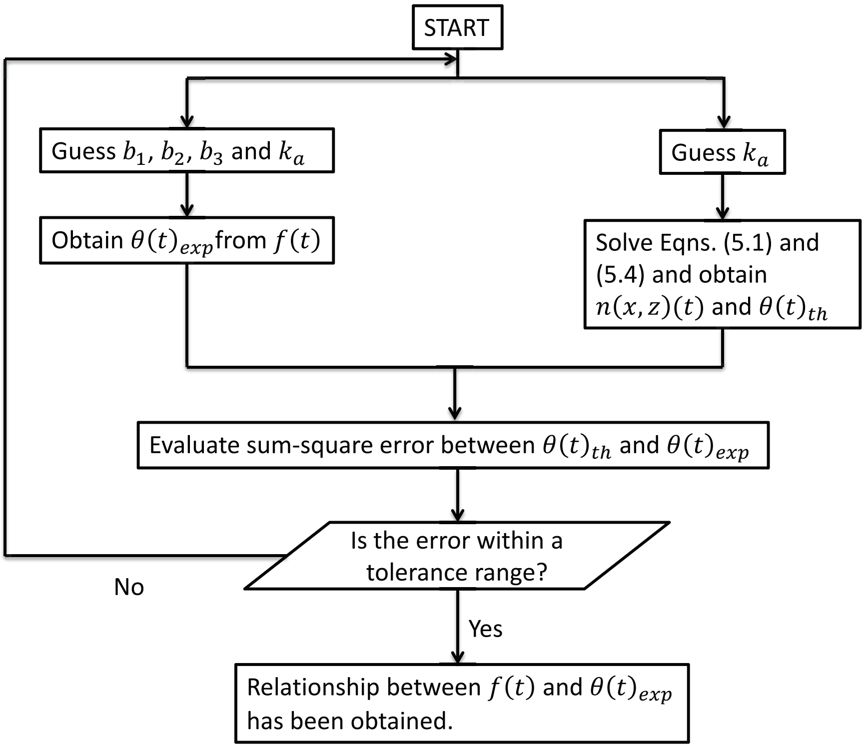

Figure 5.1: Flow chart for converting frequency shift to mass when studying nanoparticles attachment using QCM-D.

Bibliography

[1] F. Lin, L. Nolan, Z. Xu, and K. Cadien, “A study of the colloidal stability of mixed abrasive slurries and their role in CMP.” *Journal of the Electrochemical Society*, vol. 159, no. 5, pp. H482 – H489, 2012.

[2] L. Nolan and K. Cadien, “Chemical mechanical polish for nanotechnology,” in *Nanofabrication*, M. Stepanova and S. Dew, Eds. Springer Vienna, 2012, pp. 239 – 274.

[3] E. Matijevic and S. V. Babu, “Colloid aspects of chemical-mechanical planarization.” *Journal of Colloid and Interface Science*, vol. 320, no. 1, pp. 219 – 237, 2008.

[4] R. Manivannan and S. Ramanathan, “Role of abrasives in high selectivity STI CMP slurries,” *Microelectronic Engineering*, vol. 85, no. 8, pp. 1748 – 1753, 2008.

[5] W. G. America and S. V. Babu, “Slurry additive effects on the suppression of silicon nitride removal during CMP,” *Electrochemical and Solid-State Letters*, vol. 7, no. 12, pp. G327 – G330, 2004.

[6] P. W. Carter and T. P. Johns, “Interfacial reactivity between ceria and silicon dioxide and silicon nitride surfaces: Organic additive effects,” *Electrochemical and Solid-State Letters*, vol. 8, no. 8, pp. G218 – G221, 2005.

[7] S. Kim, J. H. So, D. J. Lee, and S. M. Yang, “Adsorption behavior of

anionic polyelectrolyte for chemical mechanical polishing (CMP)," *Journal of Colloid and Interface Science*, vol. 319, no. 1, pp. 48 – 52, 2008.

[8] P. R. Dandu Veera, S. Peddeti, and S. V. Babu, "Selective chemical mechanical polishing of silicon dioxide over silicon nitride for shallow trench isolation using ceria slurries," *Journal of the Electrochemical Society*, vol. 156, no. 12, pp. H936 – H943, 2009.

[9] N. Nishiguchi, T. Ueno, and M. Kawaguchi, "Polymer adsorption effects on colloidal stabilities of ceria particles and chemical mechanical polishing of silicone oxide films by ceria particles," *Journal of Dispersion Science and Technology*, vol. 31, no. 2, pp. 149 – 154, 2010.

[10] A. Jindal, S. Hegde, and S. V. Babu, "Chemical mechanical polishing of dielectric films using mixed abrasive slurries." *Journal of the Electrochemical Society*, vol. 150, no. 5, pp. G314 – G318, 2003.

[11] Z. Lu, S. Lee, V. Gorantla, S. V. Babu, and E. Matijevic, "Effects of mixed abrasives in chemical mechanical polishing of oxide films." *Journal of Materials Research*, vol. 18, no. 10, pp. 2323 – 2330, 2003.

[12] S. H. Lee, Z. Lu, S. V. Babu, and E. Matijevic, "Chemical mechanical polishing of thermal oxide films using silica particles coated with ceria," *Journal of Materials Research*, vol. 17, pp. 2744 – 2749, 2002.

[13] Z. Lu, S. H. Lee, V. R. K. Gorantla, S. V. Babu, and E. Matijevic, "Effects of mixed abrasives in chemical mechanical polishing of oxide films," *Journal of Materials Research*, vol. 18, pp. 2323 – 2330, 2003.

[14] H. Lei, F. Chu, B. Xiao, X. Tu, H. Xu, and H. Qiu, "Preparation of silica/ceria nano composite abrasive and its CMP behavior on hard disk substrate," *Microelectronic Engineering*, vol. 87, no. 9, pp. 1747 – 1750, 2010, 11th SEMATECH Surface Preparation and Cleaning Conference.

[15] P. Suphantharida and K. Osseo-Asare, "Cerium oxide slurries in CMP. Electrophoretic mobility and adsorption investigations of ceria/silicate interaction," *Journal of the Electrochemical Society*, vol. 151, no. 10, pp. G658 – G662, 2004.

[16] X. Liu, G. Chen, and C. Su, "Influence of collector surface composition and water chemistry on the deposition of cerium dioxide nanoparticles: QCM-D and column experiment approaches." *Environmental Science and Technology*, vol. 46, no. 12, pp. 6681 – 6688, 2012.

[17] B. Veriansyah, M. S. Chun, and J. Kim, "Surface-modified cerium oxide nanoparticles synthesized continuously in supercritical methanol: Study of dispersion stability in ethylene glycol medium." *Chemical Engineering Journal*, vol. 168, no. 3, pp. 1346 – 1351, 2011.

[18] A. Goldman, R. Cox, and H. Brenner, "Slow viscous motion of a sphere parallel to a plane wall-I motion through a quiescent fluid," *Chemical Engineering Science*, vol. 22, no. 4, pp. 637 – 651, 1967.

[19] ——, "Slow viscous motion of a sphere parallel to a plane wall-II couette flow," *Chemical Engineering Science*, vol. 22, no. 4, pp. 653 – 660, 1967.

[20] S. L. Goren, "The normal force exerted by creeping flow on a small sphere touching a plane," *Journal of Fluid Mechanics*, vol. 41, pp. 619–625, 4 1970.

[21] S. L. Goren and M. E. O'Neill, "On the hydrodynamic resistance to a particle of a dilute suspension when in the neighbourhood of a large obstacle," *Chemical Engineering Science*, vol. 26, no. 3, pp. 325 – 338, 1971.

[22] L. Spielman and J. Fitzpatrick, "Theory for particle collection under London and gravity forces." *Journal of Colloid and Interface Science*, vol. 42, pp. 607 – 623, 1973.

[23] T. G. M. Van de Ven, *Colloidal hydrodynamics / Theo G.M. Van de Ven.*, ser. Colloid science (London, England : 1976). London : Academic Press, 1989., 1989.

[24] J. F. Brady and G. Bossis, "Stokesian dynamics," *Annual Review of Fluid Mechanics*, vol. 20, no. 1, pp. 111 – 157, 1988.

[25] S. K. Friedlander, *Smoke, dust, and haze : fundamentals of aerosol dynamics / Sheldon K. Friedlander.*, ser. Topics in chemical engineering. New York : Oxford University Press, 2000., 2000.

[26] H. Hamaker, "The London-van der Waals attraction between spherical particles," *Physica*, vol. 4, no. 10, pp. 1058 – 1072, 1937.

[27] E. Lifshitz, "The theory of molecular attractive forces between solids." *Soviet Physics JETP*, p. 73, 1956.

[28] I. Dzyaloshinskii, E. Lifshitz, and L. Pitaevskii, "The general theory of van der Waals forces," *Advances in Physics*, vol. 10, no. 38, pp. 165 – 209, 1961.

[29] U. Hartmann, "Manifestation of zero-point quantum fluctuations in atomic force microscopy," *Physical Review B*, vol. 42, pp. 1541 – 1546, 1990.

[30] J. H. Masliyah and S. Bhattacharjee, *Electrokinetic and colloid transport phenomena / Jacob H. Masliyah, Subir Bhattacharjee.* Hoboken, N.J. : Wiley-Interscience, c2006., 2006.

[31] V. Privman, H. L. Frisch, N. Ryde, and E. Matijevic, "Particle adhesion in model systems. part 13.-theory of multilayer deposition," *Journal of the Chemical Society, Faraday Transactions*, vol. 87, pp. 1371 – 1375, 1991.

[32] N. Ryde, N. Kallay, and E. Matijevic, "Particle adhesion in model systems. part 14.-experimental evaluation of multilayer deposition," *Journal of the Chemical Society, Faraday Transactions*, vol. 87, pp. 1377 – 1381, 1991.

[33] N. Ryde and E. Matijevic, “Particle adhesion on gelatin-coated glass surfaces,” *Journal of Colloid and Interface Science*, vol. 169, no. 2, pp. 468 – 475, 1995.

[34] E. Madelung, “Das elektrische feld in systemen von regelmaBig angeordneten punktladungen,” *Physik Z.*, vol. 19, pp. 524 – 533, 1918.

[35] R. Hoppe, “Madelung constants,” *Angewandte Chemie International Edition in English*, vol. 5, no. 1, pp. 95 – 106, 1966.

[36] M. Elimelech, *Particle Deposition and Aggregation : Measurement, Modelling, and Simulation.*, ser. Colloid and Surface Engineering Series. Butterworth-Heinemann, 1998.

[37] W. B. Russel, D. A. Saville, and W. R. Schowalter, *Colloidal dispersions.*, ser. Cambridge monographs on mechanics and applied mathematics. Cambridge ; New York : Cambridge University Press, 1989., 1989.

[38] J. N. Israelachvili, *Intermolecular and surface forces.* Burlington, MA : Academic Press, 2011., 2011.

[39] R. Hogg, T. W. Healy, and D. W. Fuerstenau, “Mutual coagulation of colloidal dispersions.” *Transactions of the Faraday Society*, vol. 62, p. 1638, 1966.

[40] B. Derjaguin, “Untersuchungen ber die reibung und adhsion, iv,” *Kolloid-Zeitschrift*, vol. 69, no. 2, pp. 155 – 164, 1934.

[41] S. Bhattacharjee and M. Elimelech, “Surface element integration: A novel technique for evaluation of DLVO interaction between a particle and a flat plate.” *Journal of Colloid and Interface Science*, vol. 193, no. 2, pp. 273 – 285, 1997.

[42] H. Karimian and A. Babaluo, "Halos mechanism in stabilizing of colloidal suspensions: Nanoparticle weight fraction and pH effects." *Journal of the European Ceramic Society*, vol. 27, no. 1, pp. 19 – 25, 2007.

[43] H. J. Butt, B. Cappella, and M. Kappl, "Force measurements with the atomic force microscope: Technique, interpretation and applications." *Surface Science Reports*, vol. 59, no. 1-6, pp. 1 – 152, 2005.

[44] C. J. van Oss, R. J. Good, and M. K. Chaudhury, "The role of van der Waals forces and hydrogen bonds in hydrophobic interactions between biopolymers and low energy surfaces." *Journal of Colloid and Interface Science*, vol. 111, no. 2, pp. 378 – 390, 1986.

[45] C. J. van Oss, "Acid-base interfacial interactions in aqueous-media." *Colloids and Surfaces A: Physicochemical and Engineering Aspects*, vol. 78, pp. 1 – 49, 1993.

[46] C. J. van Oss, M. K. Chaudhury, and R. J. Good, "The mechanism of phase-separation of polymers in organic media - apolar and polar systems." *Separation Science and Technology*, vol. 24, no. 1-2, pp. 15 – 30, 1989.

[47] J. A. Brant and A. E. Childress, "Assessing short-range membrane-colloid interactions using surface energetics." *Journal of Membrane Science*, vol. 203, no. 1-2, pp. 257 – 273, 2002.

[48] C. J. van Oss, "Chapter two the apolar and polar properties of liquid water and other condensed-phase materials." *Interface Science and Technology*, vol. 16, no. The Properties of Water and their Role in Colloidal and Biological Systems, pp. 13 – 30, 2008.

[49] P. Sharma and K. Rao, "Adhesion of paenibacillus polymyxa on chalcopyrite and pyrite: surface thermodynamics and extended DLVO theory." *Colloids and Surfaces B: Biointerfaces*, vol. 29, no. 1, pp. 21 – 38, 2003.

[50] S. Bayoudh, A. Othmane, L. Mora, and H. B. Ouada, “Assessing bacterial adhesion using DLVO and XDLVO theories and the jet impingement technique.” *Colloids and Surfaces B: Biointerfaces*, vol. 73, no. 1, pp. 1 – 9, 2009.

[51] R. P. King, *Principles of flotation / edited by R.P. King.*, ser. South African Institute of Mining and Metallurgy monograph series: no. 3. Johannesburg : South African Institute of Mining and Metallurgy, 1982., 1982.

[52] M. Rodahl, F. Hook, A. Krozer, P. Brzezinski, and B. Kasemo, “Quartz-crystal microbalance setup for frequency and Q-factor measurements in gaseous and liquid environments.” *Review of Scientific Instruments*, vol. 66, no. 7, pp. 3924 – 3930, 1995.

[53] G. Sauerbrey, “Verwendung von schwingquarzen zur wgung dnner schichten und zur mikrowgung,” *Zeitschrift fr Physik*, vol. 155, no. 2, pp. 206 – 222, 1959.

[54] D. Johannsmann, “Viscoelastic, mechanical, and dielectric measurements on complex samples with the quartz crystal microbalance.” *Physical Chemistry Chemical Physics*, vol. 10, no. 31, pp. 4516 – 4534, 2008.

[55] C. Stockbridge, “Effects of gas pressure on quartz-crystal microbalances,” *Vacuum Microbalance Techniques*, vol. 5, pp. 147 – 178, 1966.

[56] T. Nomura and O. Hattori, “Short communication: Determination of micromolar concentrations of cyanide in solution with a piezoelectric detector.” *Analytica Chimica Acta*, vol. 115, pp. 323 – 326, 1980.

[57] K. K. Kanazawa and J. G. Gordon, “The oscillation frequency of a quartz resonator in contact with liquid.” *Analytica Chimica Acta*, vol. 175, pp. 99 – 105, 1985.

[58] R. K. Iler, *The chemistry of silica : solubility, polymerization, colloid and surface properties, and biochemistry / Ralph K. Iler.* New York : Wiley, c1979., 1979.

[59] D. Johannsmann, I. Reviakine, and R. P. Richter, "Dissipation in films of adsorbed nanospheres studied by quartz crystal microbalance (QCM)." *Analytical Chemistry*, vol. 81, no. 19, pp. 8167 – 8176, 2009.

[60] R. Probstein, *Physicochemical hydrodynamics : an introduction.* Hoboken, N.J: Wiley-Interscience, 2003.

[61] K. Tretiakov, K. Bishop, B. Kowalczyk, A. Jaiswal, M. Poggi, and B. Grzybowski, "Mechanism of the cooperative adsorption of oppositely charged nanoparticles." *Journal of Physical Chemistry A*, vol. 113, no. 16, pp. 3799 – 3803, 2009.

[62] A. Hanel, J. Nalaskowski, P. Satyavolu, and M. Krishnan, "Attachment of silica and alumina nanoparticles as studied by QCM," *Environmental Engineering IV*, pp. 549 – 555, 2013.

Appendices

Appendix A

MATLAB Codes to Perform DLVO and XDLVO Interaction Energy Analyses

```
1  %This code is written to obtain DLVO interaction energy curves for the
2  geometry of a sphere (i.e. ceria particle) interacting with a flat surface
3  (i.e. silica sensor).
4  %T=25°C; wt%=0.1; pH varies (the following corresponds to pH 3; for the cases
5  of pH 7 and 10, lines 17 to 20 will change as presented at the end of the
6  script).
7  %All of the parameters are introduced in their corresponding SI units.
8
9  %%%%%%%%%%%%%%%%%%%%%%%%%%%%%%%%%%%%%%%%%%%%%%%%%%%%%%%%%%%%%%%%%%%%%%%%%%%%%%
10
11 clear all; close all; clc;
12
13
14 %ceria particle diameter
15 Dp = 6 * 10^(-9);
16
17 %zeta potential of ceria particle at pH 3
18 sip = 55 * 10^(-3);
19 %zeta potential of silica surface at pH 3
20 sic = -30 * 10^(-3);
21
22 %Hamaker constant of ceria
23 A121 = 5.57 * 10^(-20);
24 %Hamaker constant of silica
25 A323 = 0.85 * 10^(-20);
26 %effective Hamaker constant for the system of ceria-water-silica
27 AH = (A121 * A323)^0.5;
28
29 %temperature
30 T = 298.15;
31
32 %%constant parameters
33 %Boltzmann constant
34 kB = 1.381 * 10^(-23);
35 %dielectric permitivity of vacuum
36 epsiz = 8.854 * 10^(-12);
37 %relative permitivity of water
38 epsir = 87.5;
39
40 %inverse Debye length
41 k = 1.4711 * 10^(8);
42
43
44 %particle-surface separation distance
45 d = 0:10^(-12):60*1*10^(-9);
46
47 %electrostaic potential
48 Upc_edl = (pi * epsiz * epsir * (Dp/2) * (sip^2 + sic^2)) * ((2*sip*sic)/
49 (sip^2+sic^2) * log ((1+exp(-k*d))./(1-exp(-k*d)))) + (pi * epsiz * epsir *
50 (Dp/2) * (sip^2 + sic^2)) * (log (1 - exp(-2*k*d)));
51
52 %van der Waals potential
53 Upc_vdW = -(AH/6)* ((Dp./(2*d)) + (Dp./(2*(d+Dp))) + log(d./(d+Dp)));
54
55 %DLVO potential
56 Upc = Upc_edl + Upc_vdW;
```

```
57   %plot normalized DLVO interaction energy versus dimensionless distance
58   y = Upc/(kB*T);
59   x = d/Dp;
60   plot(x, y);
61   grid on
62
63   %plot individual components of DLVO interaction energy versus dimensionless
64   distance (optional)
65   % hold on
66   % plot(x, Upc_edl /(kB*T));
67   % hold on
68   % plot(x, Upc_vdW /(kB*T));
69
70   %%%%%%%%%%%%%%%%%%%%%%%%%%%%%%%%%%%%%%%%%%%%%%%%%%%%%%%%%%%%%%%%%
71   %%%%%%%%%%%%%%%%%%%%%%%%%%%%%%%%%%%%%%%%%%%%%%%%%%%%%%%%%%%%%%%%%
72
73   %For the cases of pH 7 and 10, the following should replace the parameters
74   introduced at lines 17 to 20:
75
76   %zeta potential of ceria particle at pH 7
77   sip = 41 * 10^(-3);
78   %zeta potential of silica surface at pH 7
79   sic = -45 * 10^(-3);
80
81   %%%%%%%%%%%%%%%%%%%%%%%%%%%%%%%%%%%%%%%%%%%%%%%%%%%%%%%%%%%%%%%%%%%%%%%%%%%%%%%
82
83   %zeta potential of ceria particle at pH 10
84   sip = -20 * 10^(-3);
85   %zeta potential of silica surface at pH 10
86   sic = -60 * 10^(-3);
87
```

```
1   %This code is written to obtain XDLVO interaction energy curves for the
2   geometry of a sphere (i.e. ceria particle) interacting with a flat surface
3   (i.e. silica sensor).
4   %T=25°C; wt%=0.1; pH varies (the following corresponds to pH 3; for the cases
5   of pH 7 and 10, lines 17 to 20 will change as presented at the end of the
6   script).
7   %All of the parameters are introduced in their corresponding SI units.
8   
9   %%%%%%%%%%%%%%%%%%%%%%%%%%%%%%%%%%%%%%%%%%%%%%%%%%%%%%%%%%%%%%%%%%%%%%%%%%%%%
10  
11  clear all; close all; clc;
12  
13  
14  %ceria particle diameter
15  Dp = 6 * 10^(-9);
16  
17  %zeta potential of ceria particle at pH 3
18  sip = 55 * 10^(-3);
19  %zeta potential of silica surface at pH 3
20  sic = -30 * 10^(-3);
21  
22  %Hamaker constant of ceria
23  A121 = 5.57 * 10^(-20);
24  %Hamaker constant of silica
25  A323 = 0.85 * 10^(-20);
26  %Effective Hamaker constant for the system of ceria-water-silica
27  AH = (A121 * A323)^0.5;
28  
29  %temperature
30  T = 298.15;
31  
32  %%constant parameters
33  %Boltzmann constant
34  kB = 1.381 * 10^(-23);
35  %dielectric permitivity of vacuum
36  epsiz = 8.854 * 10^(-12);
37  %relative permitivity of water
38  epsir = 87.5;
39  %cut-off distance to account for Born repulsion
40  d0 = 0.158 * 10^(-9);
41  %characteristic decay length of acid-base interactions
42  lambda = 0.6 * 10^(-9);
43  %surface free energy components for ceria, silica and water
44  glp = 25.5 * 10^(-3);
45  gln = 25.5 * 10^(-3);
46  gsp = 0.8 * 10^(-3);
47  gsn = 41.4 * 10^(-3);
48  gcp = 0.21 * 10^(-3);
49  gcn = 67.73 * 10^(-3);
50  
51  %inverse Debye length
52  k = 1.4711 * 10^(8);
53  
54  %particle-surface separation distance
55  d = 0:10^(-12):6*1*10^(-9);
56  
```

```
57  %electrostaic potential
58  Upc_edl = (pi * epsiz * epsir * (Dp/2) * (sip^2 + sic^2)) * ((2*sip*sic)/
59  (sip^2+sic^2) * log ((1+exp(-k*d))./(1-exp(-k*d)))) + (pi * epsiz * epsir *
60  (Dp/2) * (sip^2 + sic^2)) * (log (1 - exp(-2*k*d)));
61
62  %van der Waals potential
63  Upc_vdW = -(AH/6)* ((Dp./(2*d)) + (Dp./(2*(d+Dp))) + log(d./(d+Dp)));
64
65  %hydration interaction energy at contact
66  G0 = (2 * (glp^0.5))*((gsn^0.5) + (gcn^0.5) - (gln^0.5)) + (2 * (gln^0.5))*(
67  (gsp^0.5) + (gcp^0.5) - (glp^0.5)) - (2)*((gsp*gcn)^0.5 + (gsn*gcp)^0.5);
68
69  %acid-base potential (i.e. hydration interaction energy)
70  Upc_AB = (4 * pi * Dp * G0 * lambda) * (exp ((d0-d)/(lambda)));
71
72  %XDLVO potential
73  Upc = Upc_edl + Upc_vdW + Upc_AB;
74
75  %plot normalized XDLVO interaction energy versus dimensionless distance
76  y = Upc/(kB*T);
77  x = d/Dp;
78  plot(x, y);
79  grid on
80
81  %plot individual components of XDLVO interaction energy versus dimensionless
82  distance (optional)
83  % hold on
84  % plot(x, Upc_edl /(kB*T));
85  % hold on
86  % plot(x, Upc_vdW /(kB*T));
87  % hold on
88  % plot(x, Upc_AB /(kB*T));
89
90  %%%%%%%%%%%%%%%%%%%%%%%%%%%%%%%%%%%%%%%%%%%%%%%%%%%%%%%%%%%%%%%%%%%%%%%%%%%%%
91  %%%%%%%%%%%%%%%%%%%%%%%%%%%%%%%%%%%%%%%%%%%%%%%%%%%%%%%%%%%%%%%%%%%%%%%%%%%%%
92
93  %For the cases of pH 7 and 10, the following should replace the parameters
94  introduced at lines 17 to 20:
95
96  %zeta potential of ceria particle at pH 7
97  sip = 41 * 10^(-3);
98  %zeta potential of silica surface at pH 7
99  sic = -45 * 10^(-3);
100
101 %%%%%%%%%%%%%%%%%%%%%%%%%%%%%%%%%%%%%%%%%%%%%%%%%%%%%%%%%%%%%%%%%%%%%%%%%%%%%%%%%%%%%%%%%%%%
102
103 %zeta potential of ceria particle at pH 10
104 sip = -20 * 10^(-3);
105 %zeta potential of silica surface at pH 10
106 sic = -60 * 10^(-3);
107
```

Appendix B

ImageJ Macro to Calculate the Radial Distribution Function (RDF)

```
// ImageJ macro to calculate the Radial Distribution Function (RDF) of
particle centers
//
// Developed by Michael Schmid (version 2008-Dec-04)
//
// This is Version 2011-08-22 (improved to fix bugs by Ajay Gopal)
//
// Input: Binary or 8-bit input image/stack with dark particles on light
background.
// Grayscale/RGB images are OK as long as "Find Maxima" works reliably on
them.
// For binary images/stacks, the macro does not care whether "black
background"
// is selected in Process>Binary>Options.
//
// Output: Normalized RDF plot with distance in pixels. For stacks the mean
is plotted.
//
// Known Issues, Updates and Examples at:
// http://imagejdocu.tudor.lu/doku.php?id=macro:radial_distribution_function
//
// Requirements: A working install of "Radial Profile" plugin is required.
Get it at
// http://rsb.info.nih.gov/ij/plugins/radial-profile.html
//
// Limitations:
// - Particle positions are rounded to full pixel nearest to particle
intensity maximum
// - RDF output distances are in pixels, irrespective of any spatial
calibration of the image
// - RDF range is 0.3x the smallest dimension of the image
// - Particles touching the edge will be ignored; this will limit the
accuracy
//    if the particles are not much smaller than the image size.
// - Do not extend the image size for avoiding edge effects; the macro takes
care of this.
//
//////////////////////////////////////////////////////////////////////////////
/////

macro "Radial Distribution Function [f5]" {
      run("Select None");
      doStack=false;
      //User dialog
      Dialog.create('RDF Options');
      Dialog.setInsets(0,0,0)
      Dialog.addMessage("Radial Distribution Function Macro \nby Michael
Schmid & Ajay Gopal \n(v.2011-08-21)");
      if (nSlices()>1) {
```

```
            Dialog.addMessage("Selected file is a stack. \nUncheck below to
analyze \nonly the current slice.");
            Dialog.addCheckbox("Use all slices in stack?", true);
      }
      Dialog.addMessage("Particle Detection Noise Threshold \nHint: test
image/s first with \nImageJ>Process>Find Maxima \nto verify that below
threshold \ngives accurate particle centers.");
      Dialog.addNumber("     Noise Threshold", 10);
      Dialog.addMessage("Default output is RDF plot with \noptions to list,
save & copy data. \nCheck below to output extra \nwindow with RDF data
table.");
      Dialog.addCheckbox("Output RDF data table ", false);
      Dialog.show;
       //Preliminary checks
      if (nSlices()>1) {doStack = Dialog.getCheckbox;}
      noiseThr = Dialog.getNumber;
      showList = Dialog.getCheckbox;
      setBatchMode(true);
      firstSlice=getSliceNumber();
      lastSlice=getSliceNumber();
      if (doStack) {
            firstSlice=1;
            lastSlice=nSlices();
      }
      width=getWidth;
      height=getHeight;
      //maxRadius may be modified, should not be larger than 0.3*minOf(width,
height);
      maxRadius=0.3*minOf(width, height);
      minFFTsize=1.3*maxOf(width, height);
      title=getTitle();
      size=4;
      while(size<minFFTsize) size*=2;
      //Main processing loop
      for (slice=firstSlice; slice<=lastSlice; slice++) {
            //Make autocorrelation of particle positions
            if (doStack) setSlice(slice);
            run("Find Maxima...", "noise="+noiseThr+" output=[Single Points]
light exclude");
            tempID=getImageID();
            tempTitle="temp-"+random();
            rename(tempTitle);
            run("Canvas Size...", "width="+ size+" height="+ size+"
position=Center zero");
            run("FD Math...", "image1=["+tempTitle+"] operation=Correlate
image2=["+tempTitle+"] result=AutoCorrelation do");
            psID=getImageID();
            selectImage(tempID);
            close();
```

```
            //Make autocorrelation reference to correct finite image size
effects
            newImage("frame", "8-bit White", width, height, 1);
            run("Set...", "value=255");
            tempID=getImageID();
            rename(tempTitle);
            run("Canvas Size...", "width="+ size+" height="+ size+"
position=Center zero");
            run("FD Math...", "image1=["+tempTitle+"] operation=Correlate
image2=["+tempTitle+"] result=AutoCorrReference do");
            refID=getImageID();
            imageCalculator("Divide", psID,refID);
            selectImage(refID);
            close();
            selectImage(tempID);
            close();
            //Prepare normalized power spectrum for radial averaging
            selectImage(psID);
            makeRectangle(size/2, size/2, 1, 1);
            run("Set...", "value=0");
            run("Select None");
            circleSize=2*floor(maxRadius)+1;
            run("Specify...", "width="+circleSize+" height="+circleSize+"
x="+(size/2+0.5)+" y="+(size/2+0.5)+" oval centered");
            getRawStatistics(nPixels, mean);
            run("Select None");
            run("Divide...", "value="+mean);
            run("Specify...", "width="+circleSize+" height="+circleSize+"
x="+(size/2+0.5)+" y="+(size/2+0.5)+" oval centered");
            run("Radial Profile", "x="+(size/2+0.5)+" y="+(size/2+0.5)+"
radius="+floor(maxRadius)-1);
            rename("RDF of "+title);
            rdfID=getImageID();
            selectImage(psID);
            close();
            //Averaging of RDFs for stacks
            if (doStack) {
                  selectImage(rdfID);
                  Plot.getValues(x, y);
                  if (slice==firstSlice) ySum = newArray(y.length);
                  for (i=0; i<y.length; i++)
                  ySum[i]+ = y[i] / lastSlice;
                  close();
            }
      }//End Processing Loop

      //Create output plots with annotated titles and options
      if (doStack) {
```

```
            Plot.create("RDF of "+title+" (stack)", "Distance (pixels)",
"RDF", x, ySum);
            if (showList) {
                  run("Clear Results");
                  for (i=0; i<x.length; i++) {
                        setResult("R", i, x[i]);
                        setResult("RDF", i, ySum[i]);
                  }
                  updateResults();
            }
      }
      else {
            selectImage(rdfID);
            Plot.getValues(x, y);
            Plot.create("RDF of "+title+" (slice"+lastSlice+")", "Distance
(pixels)", "RDF", x, y);
            if (showList) {
                  run("Clear Results");
                  for (i=0; i<x.length; i++) {
                        setResult("R", i, x[i]);
                        setResult("RDF", i, y[i]);
                  }
                  updateResults();
            }
            close();
      }//End Output
      setBatchMode("exit and display");// Comment this out if you get
duplicate RDF outputs
} //End Macro
```

Appendix C

Results of Particle Size Distribution Measurements

Figures C.1 and C.2 show two examples of the particles size distribution (PSD) results obtained by a Malvern Nano ZS Zetasizer.

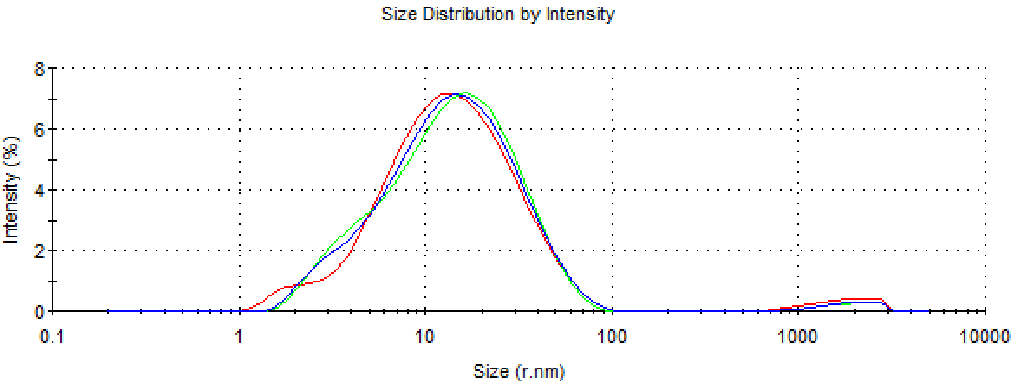

(a)

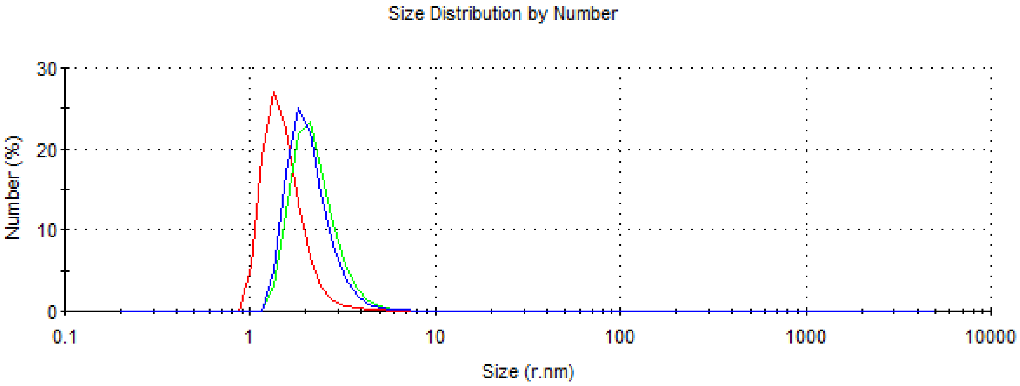

(b)

Figure C.1: PSD measurements performed by Malvern Zetasizer (three consecutive measurements acquired at normal resolution): Average Hydrodynamic Radius=10.54 nm, Radius Standard Deviation=0.02646 nm, Average Poly-Dispersity Index=0.398, Poly-Dispersity Standard Deviation=0.003.

Based on the overall hydrodynamic radius results, the average hydrodynamic radius for all the measurements is 10.62 nm. This is in agreement with the particle size of 10-20 nm provided by the supplier. However, it should be noted that although only one average hydrodynamic radius is reported by the Malvern Zetasizer, there are a number of peaks in Intensity-Size graphs (especially the ones acquired at “high resolution”) that represent more accurate information on the actual size of the particles in the slurry. According to

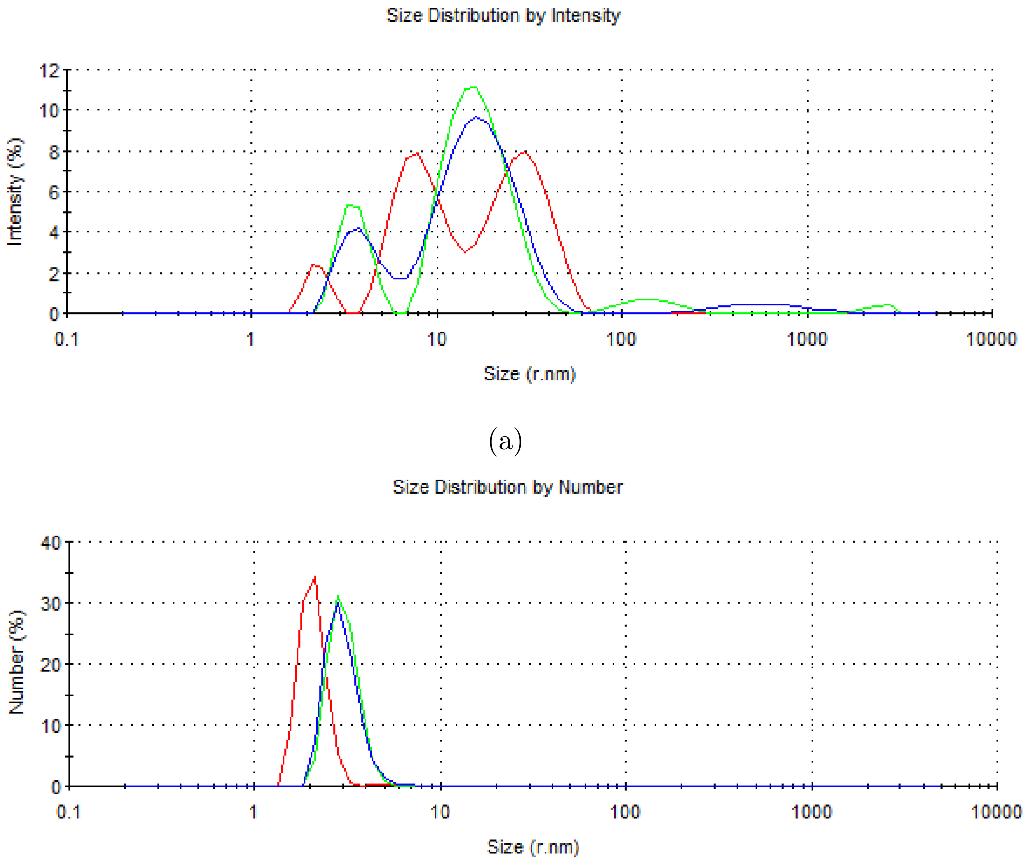

(a)

(b)

Figure C.2: PSD measurements performed by Malvern Zetasizer (another three consecutive measurements acquired at high resolution): Average Hydrodynamic Radius=10.62 nm, Radius Standard Deviation=0.09849 nm, Average Poly-Dispersity Index=0.404, Poly-Dispersity Standard Deviation=0.006.

Intensity-Size graphs, three peaks are easily distinguished.

Based on all the collected data, the three peaks in Intensity-Size graphs are approximately located at 2.93 nm, 13.02 nm, and 210.17 nm (or better to say somewhere far away from the other two) which correspond to the primary size of the NPs, growing (or moderate-size) NP aggregates, and large NP aggregates, respectively. Considering the corresponding Number-Size graphs, one can conclude that majority of NPs in the suspension have the primary size and the population of aggregates in the suspension is relatively low. This conclusion is consistent with the results of zeta potential measurements: at pH$\sim$3, average zeta potential of NPs is ∼0 mV so electrostatic interactions (repulsion) are dominant and prevent the particles to form aggregates.

It should be noted that for each set of three measurements, the first measurement is not included in calculating any of the average values because the first measurement is a tool for the device to kind of characterize the sample and optimize the upcoming [two] measurements.

In order to confirm primary size of ceria NPs and particles size distribution, measurements were repeated using a Brookhaven ZetaPALS instrument. An example of the results is shown in the figure below. Mean size distribution (MSD) is measured using a disposable clear cuvette and the same parameters as the measurements with Zetasizer. Each measurement was repeated 10 times and averaged by the instrument using the built-in software.

Again, based on ZetaPALS results, there are three peaks in Intensity-Size(diameter) graphs which correspond to the primary size of the NPs, growing (or moderate-size) NP aggregates, and large NP aggregates, respectively.

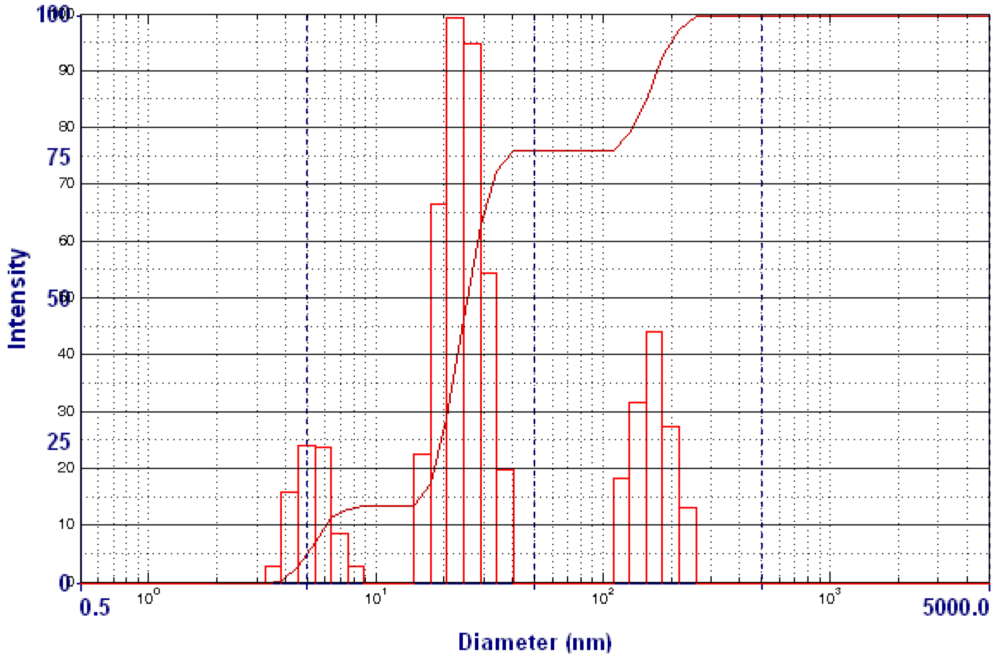

Figure C.3: PSD measurements performed by Brookhaven ZetaPALS (average of ten repeated measurements): Effective Diameter=27.3 nm, Poly-Dispersity=0.219.